Silicon-Organic Hybrid (SOH) and Plasmonic-Organic Hybrid (POH) Integration

Christian Koos, *Member, IEEE*, Juerg Leuthold, *Fellow, IEEE*, Wolfgang Freude, *Senior Member, IEEE*,
Manfred Kohl, Larry Dalton, *Senior Member, IEEE*, Wim Bogaerts, *Senior Member, IEEE*, Anna Lena Giesecke,
Matthias Lauermann, Argishti Melikyan, Sebastian Koeber, Stefan Wolf, Claudius Weimann, Sascha Muehlbrandt,
Kira Koehnle, Joerg Pfeifle, Wladislaw Hartmann, Yasar Kutuvantavida, Sandeep Ummethala, Robert Palmer,
Dietmar Korn, Alloatti Luca, Philipp Claudius Schindler, Delwin L. Elder, Thorsten Wahlbrink, and Jens Bolten

(Invited Paper)

***Abstract*—Silicon photonics offers tremendous potential for inexpensive high-yield photonic-electronic integration. Besides conventional dielectric waveguides, plasmonic structures can also be efficiently realized on the silicon photonic platform, reducing device footprint by more than an order of magnitude. However, neither silicon nor metals exhibit appreciable second-order optical nonlinearities, thereby making efficient electro-optic modulators challenging to realize. These deficiencies can be overcome by the concepts of silicon-organic hybrid (SOH) and plasmonic-organic hybrid integration, which combine SOI waveguides and plasmonic nanostructures with organic electro-optic cladding materials.**

***Index Terms*—Electro-optic modulators, nonlinear optical devices, photonic integrated circuits, plasmonics, silicon photonics.**

I. Introduction

Electro-optic (EO) modulators are key building blocks for highly integrated photonic-electronic circuits on the silicon platform [1]–[4]. Due to the absence of linear EO effects in bulk silicon, current modulators mostly rely on free-carrier dispersion (FCD) by exploiting depletion [5] or injection [6] of holes in diode or metal-oxide-semiconductor (MOS) structures [7]. However, these concepts do not allow for fast devices that feature low drive voltage and small footprint simultaneously. Carrier injection enables voltage-length products as small as $U_\pi L = 0.36$ Vmm, but the free-carrier lifetime limits the modulation speed [6]. Carrier-depletion modulators, in contrast, support symbol rates of up to 70 GBd when exploiting frequency dependent impedance mismatch to compensate for the low-pass characteristic of the device [8], but typical voltage-length products are beyond 10 Vmm [2], [9]. Similarly, high-speed plasmonic modulators predominantly exploit the interaction of surface plasmon polariton (SPP) modes with free carriers in semiconductors or metals [10]–[13], thereby suffering from limitations in speed and efficiency.

These deficiencies can be overcome by the concepts of silicon-organic hybrid (SOH) and plasmonic-organic hybrid (POH) integration, which combine silicon-on-insulator (SOI) waveguides and plasmonic nanostructures with organic EO claddings. In this paper, we review recent progress in the field of SOH [14]–[24] and POH [25]–[28] integration. The SOH concept enables highly efficient modulators having voltage-length

---

Manuscript received July 12, 2015; revised October 14, 2015; accepted November 4, 2015. This work was supported by the European Research Council (ERC Starting Grant “EnTeraPIC,” number 280145), the Alfried Krupp von Bohlen und Halbach Foundation, the EU projects PhoxTroT, BigPipes, Navolchi and SOFI, the Karlsruhe International Research School for Teratronics, the Karlsruhe School of Optics and Photonics, the Karlsruhe Nano-Micro Facility, and the Center for Functional Nanostructures of the Deutsche Forschungsgemeinschaft.

Q1 C. Koos is with the Institute of Photonics and Quantum Electronics, Institute of Microstructure Technology, Karlsruhe Institute of Technology, Karlsruhe 76131, Germany (e-mail: christian.koos@kit.edu).

J. Leuthold was with the Karlsruhe Institute of Technology, Karlsruhe 76131, Germany. He is now with the Institute of Electromagnetic Fields, Swiss Federal Institute of Technology, Zürich 8092, Switzerland (e-mail: Juerg Leuthold@ethz.ch).

W. Freude, M. Lauermann, S. Wolf, C. Weimann, and J. Pfeifle are with the Institute of Photonics and Quantum Electronics, Karlsruhe Institute of Technology, Karlsruhe 76131, Germany (e-mail: w.freude@kit.edu; matthias.lauermann@kit.edu; s.wolf@kit.edu; claudi-us.weimann@kit.edu; joerg.pfeifle@kit.edu).

A. Melikyan was with the Karlsruhe Institute of Technology, Karlsruhe 76131, Germany. He is now with Alcatel-Lucent Bell Labs, Holmdel NJ 07733, USA (e-mail: argishti.melikyan@alcatel-lucent.com).

M. Kohl, S. Muehlbrandt, K. Koehnle, W. Hartmann, Y. Kutuvantavida, and S. Ummethala are with the Institute of Microstructure Technology, Karlsruhe Institute of Technology, Karlsruhe 76131, Germany (e-mail: manfred.kohl@kit.edu; sascha.muehl-brandt@kit.edu; kira.koehnle@kit.edu; wladislaw.hartmann@kit.edu; yasar.kutuvantavida@kit.edu; sandeep.ummethala@kit.edu).

L. Dalton and D. L. Elder are with the University of Washington, Seattle, WA 20052 USA (e-mail: dalton@chem.washington.edu; elderdl@uw.edu).

W. Bogaerts is with the Photonics Research Group, Ghent University—IMEC, Ghent B-9000, Belgium and also with the Luceda Photonics, Dendermonde B-9200, Belgium (e-mail: wim.bogaerts@ugent.be).

A. L. Giesecke, T. Wahlbrink, and J. Bolten are with the AMO GmbH, Aachen 52074, Germany (e-mail: giesecke@amo.de; wahlbrink@amo.de; bolten@amo.de).

S. Koeber was with the Karlsruhe Institute of Technology,, Karlsruhe 76131, Germany. He is now with Department of Chemistry, University of Cologne, Köln 50939, Germany (e-mail: sebastian.koeber@uni-koeln.de).

R. Palmer was with the Karlsruhe Institute of Technology, Karlsruhe 76131, Germany. He is now with Coriant GmbH, Munich 81541, Germany (e-mail: robert.palmer@coriant.com).

D. Korn was with the Karlsruhe Institute of Technology, Karlsruhe 76131, Germany. He is now with Imagine Optic, Orsay 91400, France (e-mail: dietmarkorn@googlemail.com).

A. Luca was with the Karlsruhe Institute of Technology, Karlsruhe 76131, Germany. He is now with Massachusetts Institute of Technology, Research Laboratory of Electronics, Cambridge, MA 02139 USA.

P. C. Schindler was with the Karlsruhe Institute of Technology, Karlsruhe 76131, Germany. He is now with Infinera Corporation, Sunnyvale, CA 94089 USA (e-mail: pschindler@infinera.com).

Color versions of one or more of the figures in this paper are available online at http://ieeexplore.ieee.org.

Digital Object Identifier 10.1109/JLT.2015.2499763

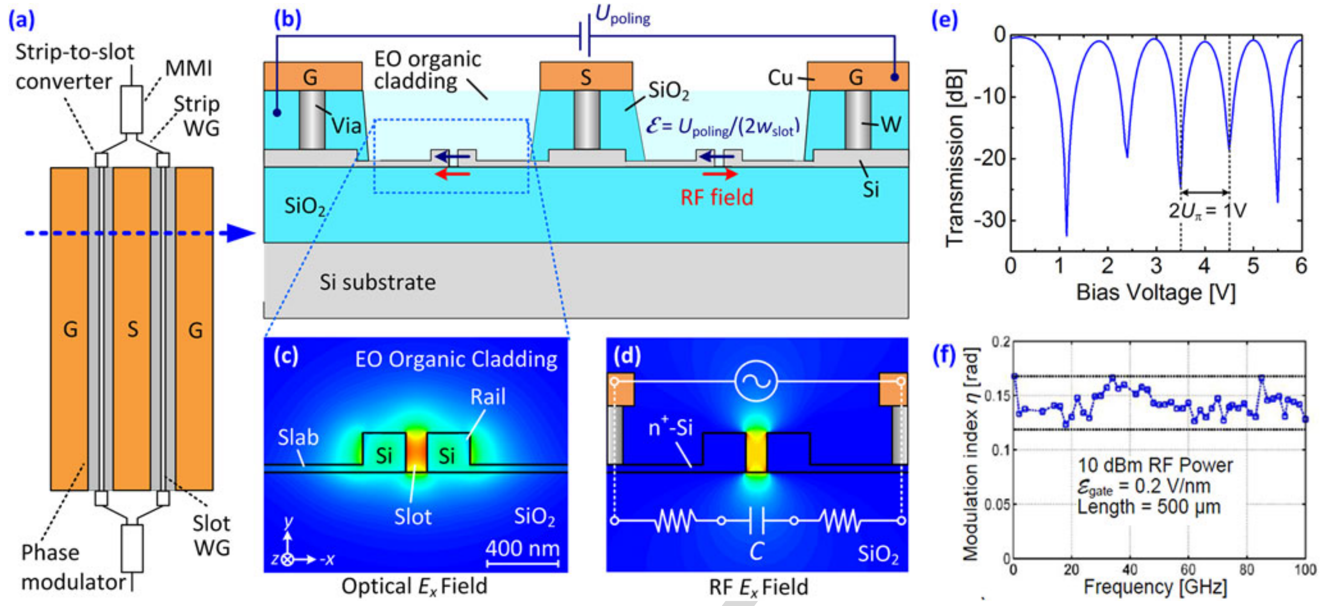

Fig. 1. Silicon-organic hybrid (SOH) MZM. (a) Schematic of the MZM. The device consists of two slot-waveguide (WG) phase modulators, driven in push-pull operation by a single coplanar GSG transmission line. Before and after the modulator sections, the light is split and combined by multimode interference couplers (MMI). (b) Cross-section of an SOH MZM using tungsten vias to connect the GSG transmission line to the Si slot waveguide. Push-pull operation is obtained by an appropriate choice of poling directions (blue arrows) of the EO cladding in both arms with respect to the direction of the local RF field (red arrows). (c) Cross-sectional view and simulated distribution of the dominant electrical component ε_x of the optical quasit-TE mode field for a single phase modulator (slot width 160 nm, rail width 210 nm, waveguide height 220 nm). The optical mode is strongly confined to the slot due to electric-field discontinuities at the slot sidewalls. (d) Simulated ε_x-component of the RF mode field of the slot waveguide. The modulation voltage drops across the narrow slot resulting in a high modulation field that has a strong overlap with the optical mode. (e) Transmission versus dc voltage of a MZM having 1 mm long phase shifters. At bias voltages above 3 V, the π-voltage of the device amounts to $U_\pi = 0.5$ V, corresponding to a voltage-length product of $U_\pi L = 0.5$ Vmm. For smaller dc voltages, free charges in the cladding lead to a partial screening of the applied electric field and hence to slightly increased π-voltages for dc operation. (f) High-speed operation: Phase modulation index η vs. frequency for an on-chip RF power of 10 dBm. When using an electric gate field E_{gate} to increase the conductivity of the slabs, a 3 dB bandwidth of at least 100 GHz can be achieved [20]. The horizontal dotted black lines represent the maximum value (upper line) and a fraction of 70.7% thereof (−3 dB, lower line). (Figure adapted from [15]).

products as small as $U_\pi L = 0.5$ Vmm [20]–[22]. SOH modulators can be designed for low energy consumptions of only a few femtojoule per bit [19], [20] or for high modulation frequencies of up to 100 GHz [21]. Moreover, SOH devices are perfectly suited for advanced modulation formats such as quadrature phase-shift keying (QPSK) and 16-state quadrature-amplitude modulation (16QAM) [22], [23]. The high modulation efficiency of SOH modulators allows to drive the devices directly from binary CMOS output ports of standard field-programmable gate arrays (FPGA) for generating advanced modulation formats without the use of digital-to-analog converters (DAC) or radio-frequency (RF) drive amplifiers [24]. POH modulators stand out due to their high modulation speed and ultra-compact footprint, featuring voltage-length products down to $U_\pi L = 0.05$ Vmm and typical lengths of a few tens of micrometers [25]–[28]. The viability of the devices has been demonstrated in a series of data transmission experiments using binary phase shift keying (BPSK), on-off-keying (OOK) and four-state amplitude shift keying (4-ASK) as modulation formats [25], [26]–[28].

The paper is structured as follows: In Section II, we introduce the principles and the unique features of SOH devices and cover a series of experimental demonstrations. Section III introduces the POH approach and summarizes the corresponding experimental demonstrations, and Section IV gives a comparison of the various modulator concepts. The paper is concluded by an outlook covering current activities and future research directions, see Section V. The Appendix gives details on mathematical models used to estimate modulator performance end efficiency.

II. SOH INTEGRATION

A. The SOH Device Concept

The basic structure of an SOH Mach–Zehnder modulator (MZM) is illustrated in Fig. 1(a) [14], [15]. The MZM comprises two SOH phase modulators that are driven in push-pull mode by a single coplanar transmission line in ground-signal-ground (GSG) configuration. Each of the phase modulators consists of a slot waveguide, which is covered by an organic EO material, see cross-section in Fig. 1(b). The fundamental optical quasi-TE mode is strongly confined to the slot region due to field discontinuities at the slot sidewalls [29], Fig. 1(c). At the same time, the metal strips of the transmission line are electrically connected to the rails of the phase modulators by thin n-doped silicon slabs such that a voltage applied to the transmission line drops across the narrow slot. This results in a strong modulating RF field that overlaps perfectly with the optical quasi-TE mode, see Fig. 1(d). For connecting the slot-waveguide phase shifters to conventional SOI strip waveguides in an MZM configuration, logarithmically tapered strip-to-slot converters are used that have insertion losses of less than 0.1 dB at lengths of less than 10 μm [30].

The basic SOI waveguide structures can be fabricated by widely available CMOS processes, and the EO organic material is then deposited by spin coating. Directly after deposition, the organic material does not show any macroscopic EO effect due to random orientation of the chromophore molecules. To induce macroscopic EO activity, the material is poled by heating it to the glass-transition temperature T_g while applying a dc poling voltage U_{poling} between the floating ground electrodes of the MZM. The resulting poling fields in the slots align the dipolar chromophores as indicated by the dark blue arrows in Fig. 1(b) [20]. While keeping the poling voltage constant, the chip is cooled back to room temperature such that the acentric order of the chromophores is conserved. The RF modulation field of the GSG transmission line, indicated by red arrows in Fig. 1(b), is parallel to the chromophore orientation in the left phase shifter and antiparallel in the phase shifter on the right-hand side, thereby resulting in efficient push-pull operation of the device.

The π-voltages of the SOH MZM are obtained from measuring the transmission as a function of an applied DC voltage, see Fig. 1(e). For a device with 1 mm-long phase shifters, we find a π-voltage U_π of only 0.5 V for bias voltages of more than 3 V, corresponding to a voltage-length product of only $U_\pi L =$ 0.5 Vmm, see Fig. 1(e) [20]. For smaller bias voltages, we observe slightly increased spacings of the transmission dips and hence slightly increased π-voltages, which is attributed to free ions in the cladding that lead to a partial screening of the applied fields at small bias voltages. This effect is only observable for low frequencies and does not impede RF operation.

The modulation speed of the modulators is limited by the *RC* time constant of the slot waveguide structure: The slot corresponds to a capacitor *C,* which is charged and discharged via the resistive silicon slabs, see Fig. 1(d). The EO bandwidth can be increased by applying a static gate voltage between the substrate and the top silicon layer, which increases the conductivity of the slabs by inducing a charge accumulation layer [31]. Applying this technique to a short device of only 500 μm length results in 3 dB bandwidths of more than 100 GHz,Fig. 1(f) [21].

The SOH approach is a general concept, which is not limited to EO modulators only. We have shown that particularly compact and power-efficient phase shifters can be realized by using liquids crystals as a cladding of the SOH waveguide [32], [33]. For a device length of 1.7 mm, we achieved an overall phase shift of approximately 80 π at a voltage of 4 V [32]. Similarly, we could demonstrate pulsed lasing in optically pumped SOH waveguides that have dye-doped polymers as a cladding [34].

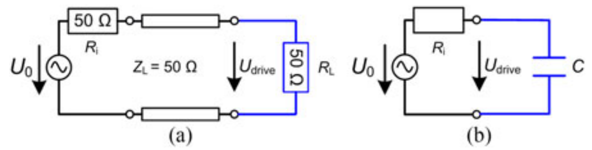

Fig. 2. Equivalent-circuit models of EO modulators. (a) Impedance-matched travelling-wave device featuring an ohmic input load impedance of $RL = 50\,\Omega$, connected to a transmission line having a wave impedance $ZL = 50\ \Omega$ and a signal source with an internal impedance of Ri.= 50 Ω. The modulator drive voltage is only half the internal source voltage, $U_{\mathrm{drive}} = U_0/2$. For estimating the energy consumption, the device is modeled by a single 50 Ω resistor. (b) Unterminated lumped-element EO modulator represented by a capacitive load *C*. If the device is driven below its $R_i C$ cut-off frequency, the drive voltage reaches a steady-state value which is equal to the open-circuit source voltage, $U_{\mathrm{drive}} = U0$. The energy consumption is then dictated by the power dissipation in the resistor R_i during charging and dis-charging the capacitor. This power dissipation is independent of the exact value of R_i.

B. Efficiency of SOH Devices

Energy efficiency is one of the most important metrics of photonic-electronic interfaces. The energy consumption of an EO modulator depends not only on the physical properties of the phase shifters, but also on the electronic design of the feed circuitry. Conventionally, modulators are designed as travelling-wave devices, having a 50 Ω input impedance, matched to the $Z_L = 50\ \Omega$ wave impedance of standard transmission lines and RF cables. For estimating the energy consumption, the device can be modeled by an equivalent circuit consisting of a single load resistor of $R_L = 50\ \Omega$, see Fig. 2(a). The driving source is characterized by an open-circuit voltage of U_0 and an internal impedance of $R_i = 50\ \Omega$ for minimum back reflection and maximum power transfer to the transmission line. The modulator drive voltage is then only half of the open-circuit source voltage, $U_{\mathrm{drive}} = U_0/2$. For simple on-off-keying, the per-bit energy consumption in the modulator can be estimated by considering the power dissipation in the load resistor during one bit slot of duration T_{bit},

$$W_{\mathrm{bit}} = \frac{U_{\mathrm{drive}}^2 T_{\mathrm{bit}}}{4R_L}. \tag{1}$$

This concept leads to comparatively high energy consumptions: For operating voltages of only $U_{\mathrm{drive}} = 1$ V, a load resistance of $R_L = 50\,\Omega$, and a data rate of 10 Gb/s, i.e., a bit duration of $T_{\mathrm{bit}} = 100$ ps, the per-bit energy consumption amounts to 500 fJ/bit.

This energy consumption can be considerably reduced by using SOH devices. First, due to highly efficient EO materials and the thereby decreased voltage-length products of $U_\pi L \approx 0.5$ Vmm, SOH phase shifters can be made much shorter than their all-silicon counterparts that rely on FCD. As a consequence, the length of SOH devices can be kept short in comparison to the RF wavelength of the modulating signal on the chip, and the devices do not need to be designed in an impedance-matched travelling-wave configuration. Instead, the modulators can be operated as purely capacitive loads, as illustrated in Fig. 2(b), assuming that the electronic driver circuitry can be co-integrated in close proximity such that the feed lines can be kept short and impedance matching is not required. Assuming that the device is driven below its $R_i C$ cut-off frequency $f_c = 1/(2\pi R_i C)$, the drive voltage reaches a steady-state value which is equal to the internal source voltage, $U_{\mathrm{drive}} = U_0$. The energy consumption is then dictated by the power dissipation in the resistor R_i during charging and discharging the capacitor. This power dissipation is independent of the exact value of R_i. For non-return-to-zero (NRZ) OOK, the power dissipation can be estimated to be [35]

$$W_{\mathrm{bit}} = \frac{C U_{\mathrm{drive}}^2}{4} = \frac{Q_{\mathrm{bit}} U_{\mathrm{drive}}}{2} \tag{2}$$

where $Q_{\mathrm{bit}} = C\, U_{\mathrm{drive}}/2$ denotes the average charge that has to be transported into the device per bit. Typical capacitances of SOH modulators amount to 200 fF for a 500 μm long device [19]. Assuming a drive voltage of 1 V, this leads to a typical per-bit energy consumption of 50 fJ/bit, which is approximately an order of magnitude smaller than the value estimated for travelling-wave devices.

Besides the operating voltage U_{drive}, Eq. (2) introduces the charge transport Q_{bit} per bit as another important figure of merit (FOM) that characterizes the efficiency of a capacitive EO phase shifter such as a reverse-biased pn-junction, an MOS capacitor, or an SOH or POH slot waveguide structure. To a first-order approximation, the phase shift in such a device is proportional to the charge transport, but independent of the device length: Increasing the length of the phase shifter will not only increase the phase shift for a given variation of refractive index and charge density, but also the active volume and hence the capacitance of the device will be increased, such that the ratio of phase shift $\Delta\varphi$ and the associated charge transfer ΔQ is constant, see Appendix for a more detailed analysis. Let us first consider a continuous-wave (CW) optical signal of vacuum wavelength λ that is phase-modulated by FCD in a silicon strip waveguide of width w and height h. Following the analysis described in the Appendix, the ratio of charge transfer and phase shift for FCD devices can be estimated to be

$$\frac{\Delta Q_{\mathrm{FCD}}}{\Delta \Phi_{\mathrm{FCD}}} = \frac{\lambda \mathrm{whe}}{2\pi B \Gamma_{\mathrm{core}}} \tag{3}$$

where $e = 1.602 \times 10^{-19}$ C is the elementary electric charge, Γ_{core} denotes the field interaction factor of the guided mode with the silicon waveguide core, and $B = 2.7 \times 10^{-21}$ cm^3 is a material constant of silicon that relates the change of the density of holes to the change of the refractive index, see Appendix. Note that the ratio of charge transfer and phase shift given in Eq. (3) is rather insensitive to the exact implementation of the device, since the parameter ranges for waveguide width w and height h are usually determined by the necessity to maintain low-loss single-mode operation of the device. For typical values of $\lambda = 1.55$ μm, $h = 220$ nm, $w = 450$ nm, and $\Gamma_{\mathrm{core}} = 0.8$, we obtain charge transfers of the order of $\Delta Q_{\mathrm{FCD}}/\Delta\phi_{\mathrm{FCD}} \approx 6$ pC/π for devices that are based on FCD.

Similarly, we can estimate the normalized charge transfer for an SOH device, clad by an organic EO material of optical refractive index n_{EO}, EO coefficient r_{33}, and an RF dielectric constant ε_r, see Appendix for more details. In this case, the ratio of charge transfer and phase shift amounts to

$$\frac{\Delta Q_{\mathrm{SOH}}}{\Delta \Phi_{\mathrm{SOH}}} = \frac{\lambda \varepsilon_0 \varepsilon_r h}{2\pi r_{33} n_{\mathrm{EO}}^3 \Gamma_{\mathrm{slot,x}}} \tag{4}$$

where $\varepsilon_0 = 8854 \times 10^{-12}$ As/Vm denotes the vacuum permittivity, and $\Gamma_{\mathrm{slot},x}$ is the field interaction factor of the E_{x}-component of the guided mode field with the EO material in the slot, see Eq. (20) of the Appendix for the mathematical relationship and Fig. 8(a) for numerically calculated values. Also here, the ratio of charge transfer and phase shift is rather insensitive with respect to the device geometry, given the fact that there is only limited flexibility of choosing the height h of a single-mode SOI waveguide. For typical values of $\lambda = 1.55$ μm, $n_{\mathrm{EO}} = 1.7$, $r_{33} = 150$ pm/V, $h = 220$ nm, $\varepsilon_r = 6$, and $\Gamma_{\mathrm{slot},x} = 0.25$, we obtain charge transfers of the order of $\Delta Q_{\mathrm{SOH}}/\Delta\phi_{\mathrm{SOH}} \approx 50$ fC/π. This means that for a given phase shift the charge transport required in an SOH device is more than two orders of magnitude smaller than that for a conventional silicon photonic device relying on FCD. This figure is independent of the length and hence independent of the operation voltage of the device. This confirms the superior efficiency of the SOH approach. Note that the ratio $\Delta Q_{\mathrm{SOH}}/\Delta\phi_{\mathrm{SOH}}$ derived for SOH devices also applies to POH modulators, see Appendix. A more detailed comparison of different FOM for SOH, POH, and FCD modulators is given in Section IV.

C. Advanced EO Materials

Besides the design of the optical waveguide and of the RF feed line, the EO properties of the cladding are of crucial importance for the performance of SOH modulators. Conventionally, the most commonly used cladding materials for SOH integration are polymers doped with EO chromophores [36], [37]. While these guest-host materials exhibit EO coefficients r_{33} as high as 198 pm/V at a wavelength of 1550 nm in bulk material or stacked thin-film layers [38], [39], values measured in SOH devices were much smaller, ranging from 20 to 60 pm/V [36], [37]–[40]. We demonstrated that significantly larger in-device EO coefficients of up to 230 pm/V can be achieved by using monolithic or binary chromophores that do not require a polymer matrix to mitigate dipolar interaction and detrimental head-to-tail orientation of the chromophore molecules [19]. Fig. 3(a), (b), and (c) show different molecular structures of EO materials. YLD124 is an EO chromophore that is usually used in conventional guest-host systems [41], [42], whereas the chromophores DLD164 and PSLD41 are structurally engineered molecules optimized for enhanced poling efficiency when used in monolithic form. For DLD164, Fig. 3(b), pendant coumarin-containing site-isolation groups (depicted in blue) mitigate dipole-dipole interaction and reduce the rotational degrees of freedom of the chromophores from three to two. This improves the chromophore alignment for a given poling field by roughly a factor of two [39]. For PSLD41, Fig. 3(c), perfluoraryl-containing side-groups ("site-isolation groups," depicted in blue) are used to effectively reduce the dipole-dipole interaction of neighboring molecules. The chromophore features a dendrimer structure, consisting of a central connecting motif that links three EO substructures. This results in a spherical shape of the molecule and improved poling efficiency [43].

To investigate the performance of these materials in SOH devices, we apply them to nominally identical modulator chips and measure the π-voltage at dc such that the EO coefficient r_{33} can be derived. Fig. 3(d) depicts the resulting r_{33} as a function of the applied poling field for various materials. This allows calculating the poling efficiency, i.e., the ratio $r_{33}/E_{\mathrm{poling}}$ in the limit of small poling fields, indicated by the straight fitted lines in Fig. 3(d). For a guest-host system of YLD124 (25 wt.%)

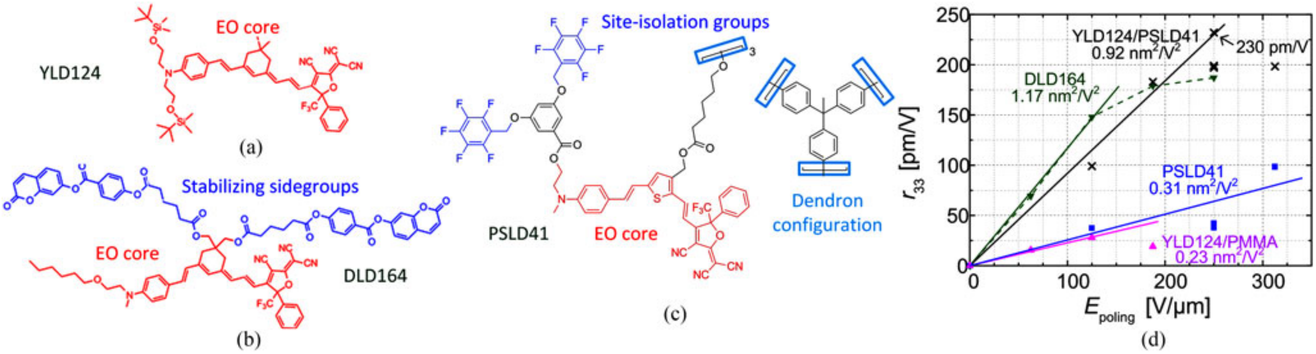

Fig. 3. (a)–(c) Chemical structures of EO chromophores. The EO active cores are drawn in red. The materials DLD164 and PSLD41 consist of structurally engineered chromophores that enable high chromophore densities and a high degree of chromophore orientation during poling. Sidegroups that lead to matrix stabilization and enhancement of molecular orientation are marked in blue. (a) YLD124, used in guest-host systems (PMMA doped with 25 wt% YLD124) or in a binary-chromophore organic glass together with PSLD41 (25:75 wt%). (b) DLD164, used in pure form as a monolithic chromophore. (c) PSLD41, a dendritic molecule that combines three EO substructures, marked in light blue. (d) Measured poling efficiencies r_{33} / E_{poling} for the different organic cladding materials. We find extraordinarily high in-device EO coefficients for DLD164 (190 pm/V) and for the YLD124/PSLD41 mixture (230 pm/V). (Figure adapted from [16]).

in PMMA, we measure small r_{33}-values of less than 29 pm/V only along with low poling efficiencies of 0.23 nm^2/V^2. These values are far below those achieved in the corresponding bulk material [38] and similar to previously reported results in other guest-host systems [36]–[44]. For the pure monolithic chromophore DLD164, we find a much higher poling efficiency of 1.17 nm^2/V^2 and a large r_{33} of up to 190 pm/V, see green trace in Fig. 3(d). For pure PSLD41, both the in-device r_{33} and the poling efficiency are slightly smaller and amount to 97 pm/V and 0.31 nm^2/V^2, respectively, whereas a mixture of YLD124 and PSLD41 (25:75 wt.%) results in an EO coefficient of 230 pm/V which is even higher than that of its constituents with a poling efficiency of 0.92 nm^2/V^2. These findings are in good agreement with results obtained in the corresponding bulk material, where the binary chromophore system YLD124/PSLD41 was found to have an r_{33} coefficient that exceeds even the sum of the r_{33} coefficients of its constituents [45]. The observed r_{33} coefficient of 230 pm/V is the highest reported value in an SOH device until now, and is even higher than previously reported record values of a fully organic MZM, where 137 pm/V was measured [46].

Comparing in-device EO coefficients r_{33} to the values obtained for the corresponding EO bulk materials, we find that poling efficiencies r_{33}/E_{poling} for bulk material are generally higher than for thin layers in SOH devices. However, the thin layers of EO material in SOH devices turn out to be more resilient with respect to dielectric breakdown, such that higher electric poling fields E_{poling} can be applied than in bulk configurations. We attribute the increased resilience to thin-film effects and to a low number of defects in the SOH slot region. The ability to use higher poling fields may even overcompensate the effect of a reduced poling efficiency: For PSLD41, the highest reported bulk EO coefficient amounts to $r_{33} = 90$ pm/V and is achieved for a poling field of 90 V/μm, whereas an r_{33}-coefficient of 98 pm/V was observed in an SOH device for a poling field of more than 300 V/μm, which is far beyond the maximum applicable poling field of 100 V/μm in bulk material. A more detailed discussion can be found in [19].

D. Advanced EO SOH Devices: Modulation at fj/bit and Advanced Modulation Formats

The viability of SOH devices has been demonstrated in a series of experiments. By combining highly efficient EO materials with ultra-short devices that can be operated as purely capacitive loads, MZM with record-low power consumptions were demonstrated [19], [20]. In an OOK signaling experiment, a peak-to-peak drive voltage of only 80 mV$_{\text{pp}}$ was sufficient to keep the measured bit-error ratio (BER) below the hard-decision forward-error correction (FEC) threshold of 4.510^{-3} [47]. This corresponds to a record-low energy consumption of only 0.7 fJ/bit [20]. For a BER below 10^{-9}, a drive voltage of $U_{\text{drive}} = 460$ mV$_{\text{pp}}$ was required, corresponding to a power consumption of 27 fJ/bit. An eye diagram for a peak-to-peak drive voltage of 300 mV$_{\text{pp}}$ is depicted in Fig. 4(a), corresponding to an energy consumption of 10 fJ/bit. These figures are an order of magnitude below the energy consumption of all-silicon MZM relying on FCD [48]. Besides conventional OOK, SOH MZM also support advanced modulation formats such as binary phase shift keying (BPSK) and bipolar amplitude shift keying (ASK), Fig. 4(b) [17]. Using bipolar 4ASK at a symbol rate of 64 GBd, we demonstrated line rates of up to 128 Gb/s [49]. Moreover, QPSK and 16-state quadrature amplitude modulation (16QAM) have been demonstrated with symbol rates (raw data rates) of up to 45 GBd (90 Gb/s) and 40 GBd (160 Gb/s), respectively, see Fig. 4(c) and (d) [22]–[24]. For 16QAM transmission at 28 GBd, the IQ modulator was operated with peak-to-peak drive voltages of 600 mV$_{\text{pp}}$, leading to a power consumption of only 19 fJ/bit [22]. This is the lowest drive voltage and the lowest energy consumption that has so far been reported for a silicon 16QAM modulator at comparable speed.

The high modulation efficiency of SOH devices can be used to greatly simplify the electronic driver circuitry. In particular, it is possible to directly use the binary outputs of state-of-the-art CMOS circuitry for generating the sub-1 V drive signals required to operate the modulator. We have demonstrated generation of simple OOK signals by connecting an SOH MZM

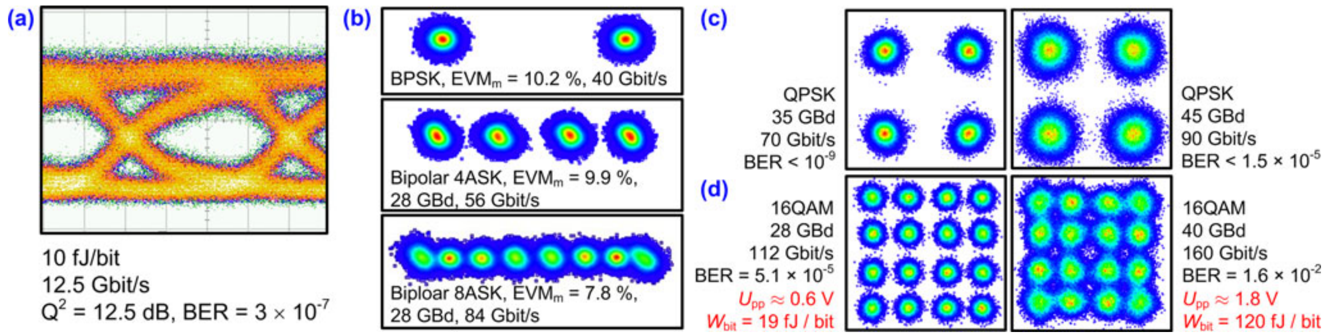

Fig. 4. Experimental demonstration of high-performance SOH modulators. (a) Modulation at ultra-low energy consumption: When operating a short device with high EO efficiency as a capacitive load, good signal quality can be obtained for modulation energies of a few femtojoule per bit [19], [20]. (b) Constellation diagrams for BPSK and bipolar ASK along with the corresponding error-vector magnitudes (EVM). BPSK transmission was found to be error-free. For the bipolar 4ASK (56 Gb/s) and the bipolar 8ASK (84 Gb/s), the measured BER amounted to 2×10^{-6} and 9.7×10^{-3}, respectively [17]. (c) Constellation diagrams of QPSK signals for symbol rates of 35 and 45 GBd [22], [23]. No bit errors were detected within our record length of 62.5 μs for 35 GBd, and the error vector magnitude ($\mathrm{EVM_m}$) indicate error-free signals with BER $< 10^{-9}$. At 45 GBd, the BER amounts to 1.5×10^{-5} and is well below the threshold for hard-decision FEC with 7% overhead. (d) Constellation diagrams of 16QAM-signals for symbol rates of 28 and 40 GBd. For 28 GBd, the IQ modulator was operated with peak-to-peak voltages of $U_{\mathrm{pp}} = 0.6$ V, leading to a power consumption of 19 fJ/bit and a BER of 5.1×10^{-5}—well below the threshold for second-generation hard-decision FEC. For 40 GBd, the BER is still below the 2.4×10^{-2} threshold for soft-decision FEC with 20 % overhead. (Figure adapted from [15]).

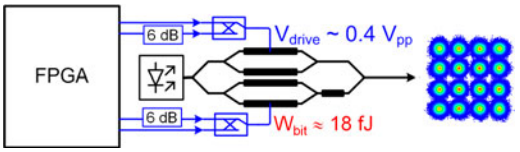

Fig. 5. DAC-less amplifier-less generation of 16QAM signals by driving a highly efficient SOH IQ modulator from the binary CMOS outputs of a FPGA via a purely passive combiner network. The four-level drive signals for the in-phase (I) and quadrature (Q) arm of the modulator are generated by superimposing two binary signals, one of which is attenuated by a factor 2 in amplitude (6 dB). The resulting four-level signal has a peak-to-peak amplitude of 400 m V_{pp}. and is sufficient to generate high-quality 16QAM signals at a symbol rate of 10 GBd and an energy consumption of only 18 fJ/bit [24].

directly to a standard 10 Gb/s GTX transmitter port of a Xilinx Virtex-7 FPGA without using an intermediate drive amplifier [50]. More recently, we have extended this concept to advanced modulation formats by demonstrating that 16QAM signals at 13 GBd can be generated without using DAC or drive amplifiers [24]. The underlying concept is illustrated in Fig. 5. A highly efficient SOH IQ modulator is connected to four binary CMOS outputs of a FPGA via a purely passive combiner network. The four-level drive signals for the in-phase (I) and quadrature (Q) MZM are generated by a purely passive combiner network which superimposes two binary signals, one of which is attenuated by a factor 2 in amplitude (6 dB). The resulting four-level signal has a peak-to-peak amplitude of 400 $\mathrm{mV_{pp}}$, which is sufficient to generate 16QAM signals that maintain a BER below the threshold of hard-decision FEC with 7% overhead, even after propagation over 100 km [24]. The associated energy consumption amounts to only 18 fJ/bit and is smaller by more than an order of magnitude than that of conventional 16 QAM transmitters.

III. POH INTEGRATION

A. The POH Device Concept

The basic idea of the SOH concept can be transferred to plasmonic waveguides, leading to POH devices. In POH phase shifters, both the optical and the RF signal are guided by thin metal sheets, see Fig. 6(a) and (b) [25]. The two sheets form a metal slot waveguide in which light propagates as a SPP mode. The slot is filled with an EO polymer, and phase modulation is achieved by applying a voltage to the metal sheets. The tight confinement of the SPP modes leads to an overlap of optical and RF field that is even better than for POH waveguides. As a consequence, record-low voltage-length products down to $U_\pi L = 0.05$ Vmm were demonstrated in POH devices [27]. Moreover, POH modulators offer speed advantages compared to their SOH counterparts: In SOH devices, charging and discharging of the slot capacitance through the resistive silicon slabs leads to an intrinsic *RC* time constant which may limit the speed of the device as described in Section II-A [21]. POH devices are not affected by such intrinsic limitations, since the slot capacitance is connected to the source by a highly conductive metal film, within which free carriers rearrange virtually instantaneously under the influence of an externally applied voltage. Moreover, extrinsic speed limitations caused by a nonzero internal impedances of real-world voltage sources can be safely neglected in POH devices due to the extraordinarily small capacitance, which can be of the order of $C = 3$ fF [27]. Together with an internal source impedance of typically $R_i = 50\ \Omega$, this leads to an *RC*-related bandwidth of the order of 1 THz, which is far above the limitations imposed by current electronic drive circuitry. This in combination with the essentially instantaneous response of the organic EO cladding material frees POH devices from any appreciable limitations of the modulation speed.

Since plasmonic waveguides still exhibit substantial propagation loss, it is advantageous to embed the POH into a network of conventional dielectric SOI waveguides that allow low-loss transport of light across the photonic chip, see Fig. 6(c). For efficient mode conversion between the photonic strip waveguide and the plasmonic slot waveguide, transitions between the dielectric transport waveguides and the POH phase shifter sections are realized by inversely tapered SOI structures that connect to the input of a tapered SPP slot waveguide, Fig. 6(d) [25]. The coupling structures are approximately 3 μm long and feature power conversion efficiencies of more than 80% [25].

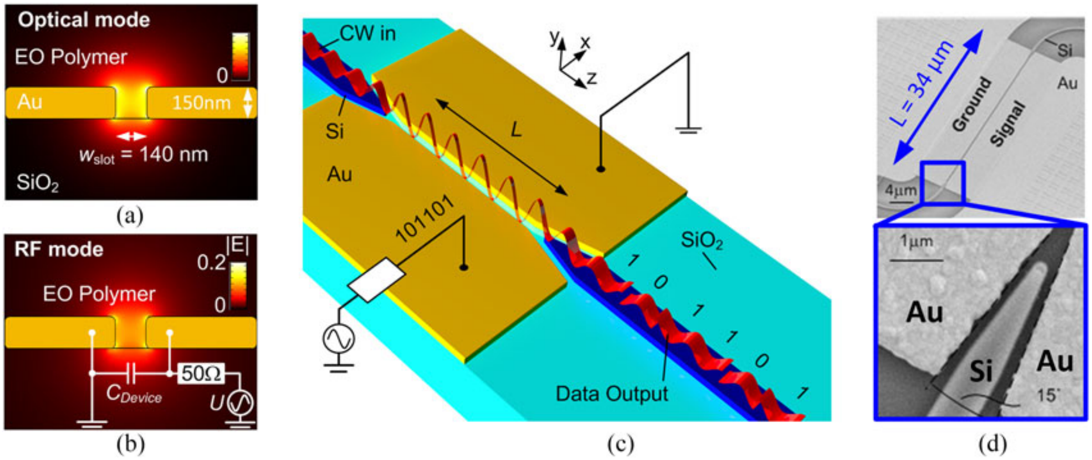

Fig. 6. POH phase modulator. (a) Optical mode: Light is guided as a SPP mode of a metal slot waveguide. The slot is filled with an EO polymer, and phase modulation is achieved by applying a modulating voltage to the metal sheets. (b) RF mode: The applied voltage drops entirely across the slot, leading to perfect overlap of the RF mode with the optical mode in the EO cladding. (c) POH modula-tor connected to dielectric SOI waveguides: Current plasmonic waveguides feature high propagation losses. It is therefore advantageous to embed the POH phase modulator into conventional silicon photonic circuitry that uses low-loss dielectric waveguides to transport light across the chip. (d) Mode converter between a photonic strip waveguide and a plasmonic slot waveguide made from gold (Au). The converter structures are approximately 3 μm long and feature power conversion efficiencies of more than 80 %. (Figure modified from [25]).

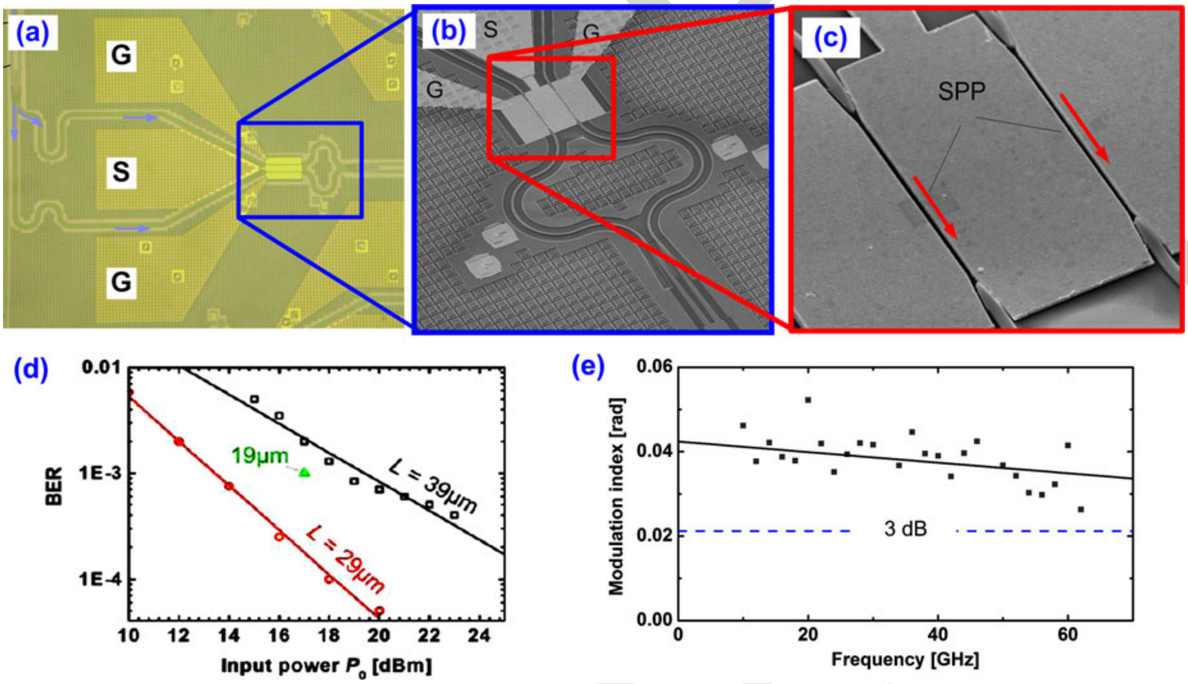

Fig. 7. Experimental demonstration of a POH MZM. (a) The POH phase shifters are embedded into a Mach–Zehnder interferometer realized by conventional SOI strip waveguides. Electrical signals are fed to the device using a GSG electrode configuration. (b), (c) Zoom-in of the POH phase shifters and the transitions between dielectric SOI waveguides and plasmonic slot waveguides. (d) BER versus optical input power $P0$ into the POH MZM for different phase shifter lengths L. A phase shifter length of $L = 29$ μm leads to a compromise between the optical insertion loss and the modulation depth of the signal. (e) Frequency response of a 29 μm-long POH phase modulator. The graph depicts the modulation index as a function of the modulating frequency for a sinusoidal RF modulation signal delivered by a 50 Ω generator with an available power of –10 dBm. Grey dots indicate measured values, and the black line represents a linear fit to this data. The frequency response is essentially flat over the measurement range, except for a small frequency-dependent decay and some oscillations that we attribute to reflections from the POH modulator that acts as a capacitive load. To indicate the 3 dB limit, we include a dashed line at half the modulation index in the low-frequency limit. The device features a 3 dB bandwidth of significantly more than 60 GHz.

B. Experimental Demonstrations of POH Devices

The viability of POH EO modulators was demonstrated in first data transmission experiments using BPSK and conventional on-off keying (OOK) at data rates of 40 Gb/s as well as bipolar ASK with four levels (4ASK) at 90 Gb/s [25]–[28]. The MZM device layout and the experimental results for 40 Gb/s OOK are depicted in Fig. 7 [26]. The device consists of a Mach–Zehnder interferometer realized by conventional SOI strip waveguides with embedded POH phase shifter sections, see Fig. 7(a), (b), and (c).

Electrical signals are fed to the device by GSG electrodes, and appropriate poling of the POH phase shifters is used to enable

TABLE I
COMPARISON OF FOM OF DIFFERENT MODULATOR TYPES

Modulator Type	$U_\pi L$ [Vmm]	a [dB/mm]	$aU_\pi L$ [dBV]	ΔQ/Δφ[fC/π]	$W_{\pi,1\,\mathrm{dB}}$, [fJ]
pn-depletion	10.00	1	10	> 1000	5000
SOH	0.5	2	1	50	25
POH	0.05	200	10	12	60

efficient push-pull operation as described for SOH devices in Section II-A. The performance of the generated data signal depends predominantly on the length L of the phase shifters: Giving the limited RF drive power, short devices lead to an insufficient modulation depth, whereas long devices suffer from excessive optical insertion loss and hence degrade the signal quality as well.Fig. 7(d) shows measured BER versus optical input power P_0 that is launched into MZM of different phase shifter lengths L. A length of $L = 29\ \mu$m leads to the lowest BER for a given launch power and hence represents a good compromise between the optical insertion loss and the modulation depth of the signal. To characterize the high-speed behavior of the device, we measured the EO response of a 29 μm long POH phase modulator, see Fig. 7(e) which depicts the modulation index as a function of the modulation frequency for a 29 μm-long POH phase modulator. The device was driven by sinusoidal signal generator having an impedance of 50 Ω and an available RF power of –10 dBm. Grey dots indicated measured values, and the black line represents a linear fit to the measured data. The frequency response features a small frequency-dependent decay and some oscillations that we attribute to back-reflections due to the capacitive input impedance of the POH modulator. The 3 dB bandwidth of the device is significantly larger than the measurement range of 60 GHz. The decay of the frequency response is attributed to RC time constants that result from an interaction of the device capacitance with the 50 Ω internal impedance of the source and additional parasitic impedances of the feed circuitry.

IV. COMPARISON OF DEVICE CONCEPTS AND PERFORMANCE

When evaluating the performance of POH modulators in comparison to SOH devices and conventional depletion-type FCD modulators, several FOM need to be considered, see Table I. Note that for all FOM described in this section, smaller values correspond to superior device performance. This somewhat counter-intuitive definition of the FOM is chosen to adhere to conventional modulator performance metrics that are commonly used in the literature. Modulator efficiency is normally expressed by the product of π-voltage U_π and device length L. In this respect, current SOH devices show more than an order of magnitude of improvement [20] compared to conventional depletion-type FCD modulators [2]–[9]. POH devices improve this FOM by another order of magnitude [27] due to an enhanced interaction of the guided light and the RF modulation field within the EO material. For a more detailed quantitative analysis of the enhanced interaction, we consider the phase shift $\Delta\varphi$ accumulated along a phase-shifter waveguide of length L under the influence of an externally applied voltage,

$$\Delta\Phi = -k_0 \Delta n_\mathrm{e} L. \tag{5}$$

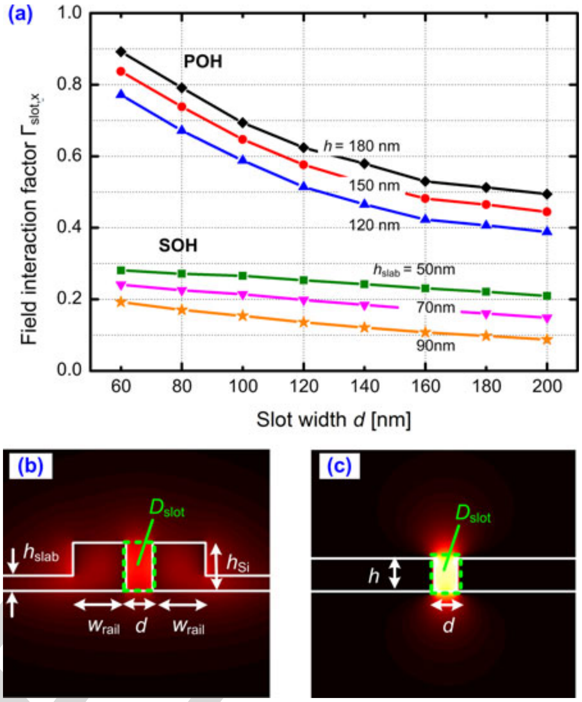

Fig. 8. Field interaction of the optical mode with the EO cladding material. (a) Field interaction factor γ_slot of the optical mode with the EO cladding material in the slot region D_slot as a function of slot width d for both POH and SOH waveguides at a wavelength of 1550 nm. The field interaction factor $\gamma_\mathrm{slot,x}$ as defined in Eq. (20) of the Appendix takes into account both the effects of spatial field overlap and of reduced group velocity. For the SOH device, the height of the silicon waveguides amounts to $hSi = 220$ nm, and a value of $w_\mathrm{rail} = 240$ nm was chosen for the width of the silicon rails, which represents approximately the optimum for a maximum field interaction factor $\gamma_\mathrm{slot,x}$. In general, POH devices feature a 2.5–3.5 times larger field interaction factor than SOH devices due to the tight confinement of the plasmonic mode to the slot region and due to a reduced group velocity of the plasmonic slot mode. For POH devices, $\gamma_\mathrm{slot,x}$ decreases as the height h of the metal is reduced, since the mode field reaches further out of the slot region D_slot. Similarly, for SOH devices, γ_slot decreases as the height h_slab of the silicon slabs is increased, since the optical mode field reaches out further into the slab region and the intensity within D_slot reduces. For the width of the silicon rails, the optimum value of $w_\mathrm{rail} \approx 240$ nm represents a trade-off between strong field confinement in the silicon core for very wide rails and deep penetration of the mode field into the cladding for very narrow rails. (b) Cross section and mode field of an SOH phase shifter ($h_\mathrm{Si} = 220$ nm, $w_\mathrm{rail} = 240$ nm, $d = 120$ nm, $h_\mathrm{slab} = 70$ nm); (c) Cross section and mode field of a POH phase shifter ($h = 150$ nm, $d = 100$ nm). The quasi-TE mode of the POH structure features a significantly stronger confinement to the slot region than its SOH counterpart.

In this relation, $k_0 = 2\pi c/l$ is the optical vacuum wavenumber at a vacuum wavelength λ, and Δn_e denotes the change of the effective refractive index $n_e = \beta/k_0$ of the waveguide mode as a consequence of the applied modulation voltage U. For both SOH and POH devices, Δn_e can be approximately expressed by the voltage U, the EO coefficient r_{33} of the cladding material, the slot width d, and the field interaction factor $\Gamma_\mathrm{slot,x}$of the E_x-component of the optical quasi-TE mode with the EO material in the slot region D_slot, see Fig. 8 (b) and (c) and Eqs. (18)–(20) of the Appendix. This leads to the relation

$$\Delta\Phi = \frac{1}{2} n_\mathrm{EO}^3 r_{33} \frac{U}{d} \Gamma_\mathrm{slot,x} k_0 L \tag{6}$$

where n_EO denotes the refractive index of the EO cladding without any voltage applied to the device, and where $\Gamma_\mathrm{slot,x}$is given by Eq. (20) in the Appendix. From these relations, we can derive the voltage-length product required to obtain a phase shift of π,

$$U_\pi L = \frac{2\pi d}{n_{\mathrm{EO}}^3 r_{33} k_0 \Gamma_{\mathrm{slot,x}}}. \tag{7}$$

For a given EO material, POH devices feature a smaller $U_\pi L$ FOM due to the fact that the field interaction factor $\Gamma_{\mathrm{slot,x}}$ of the optical mode with the slot region of POH devices can be 2.5 − 3.5 times larger than for SOH devices, see Fig. 8(a). This is due to both the tight confinement of the plasmonic mode to the slot region, see Fig. 8(b) and (c), and the reduced group velocity of the plasmonic slot waveguide mode. Note that the field interaction factor $\Gamma_{\mathrm{slot,x}}$ as defined in Eq. (20) of the Appendix already accounts for effects of group velocity.

Another important FOMof EO modulators results from the fact that the device length is related to the insertion loss via the propagation loss a in the phase shifter section. The quantity a is usually expressed in dB/mm. For pn-depletion-type phase shifters, propagation losses are mainly caused by doping, and typically amount to approximately 1 dB/mm. For SOH devices, doping doses can be kept lower in the active region of the waveguide, and the associated propagation losses are expected to stay below 1 dB/mm. In addition, SOH devices experience structure-related propagation losses, which are attributed to sidewall roughness of the slot waveguides. It has been shown that asymmetric slot waveguides and optimized fabrication techniques can reduce structure-related propagation losses to less than 1 dB/mm [51]. For the overall propagation loss of a doped slot waveguide after optimization, we hence estimate an upper boundary of 2 dB/mm—slightly worse than for the pn-depletion-type device. Plasmonic slot waveguides have considerably higher losses of the order of 400 dB/mm for current devices based on Au structures [26], which might be reduced to 200 dB/mm by replacing Au with Ag [28]. In this context, it is important to consider that POH devices are significantly shorter than their SOH or depletion-type counterparts, which strongly mitigates the loss issue. This is expressed by the product of the propagation loss a and the $U_\pi L$ FOM—see fourth column in Table I. The resulting π-voltage-loss product has the unit dB V; it corresponds to the product of the phase-shifter insertion loss and the π-voltage and can be interpreted as the π-voltage of a device having a 1 dB insertion loss or, equivalently, as the insertion loss of a device having a π-voltage of 1 V. The SOH devices feature the lowest π-voltage-loss product $aU_\pi L \approx 1$ dB V, whereas the corresponding numbers for both depletion-type devices are one order of magnitude higher. Interestingly, due to their small voltage-length product, POH modulators show similar performance as depletion-type modulators regarding the π-voltage-loss product. The fifth column of Table I specifies the charge ΔQ that has to be transferred to the device to achieve a phase shift of $\Delta\phi = p$. As explained in Section II-B and in the Appendix, this number is rather insensitive to the exact implementation of the device and can therefore be taken as an FOM for the efficiency of the underlying phase modulation mechanism. For SOH devices, a ratio of $\Delta Q/\Delta\phi \approx 50$ fC/π was estimated according to Eq. (4) in Section II-B using typical values of $\lambda = 1.55\ \mu$m, $n_{\mathrm{EO}} = 1.7$, $r_{33} = 150$ pm/V, $h = 220$ nm, $\varepsilon_r = 6$, and $\Gamma_{\mathrm{slot},x} = 0.25$. The same relation can be used for POH devices, but with a reduced thickness $h = 150$ nm of the metal layer and an enhanced field interaction factor of the order of $\Gamma_{\mathrm{slot},x} = 0.70$. This leads to a ratio of $\Delta Q/\Delta\phi \approx 12$ fC/π. All these numbers are to be understood as estimates indicating the order of magnitude—for FCD, our analysis given in Section II-B leads to a value of $\Delta Q/\Delta\phi \approx 6000$ fC/π, where optimization of the optical mode overlap with the doping was not yet considered.

Combining the aforementioned FOM, we can also quantify the power consumption of the various modulator types. For comparability, we consider devices having an insertion loss of 1 dB, hence requiring an operation voltage of $U = aU_\pi L/1$ dB to produce a phase shift of π. At the same time, we can calculate the charge transport associated with a π phase shift to be $Q = \Delta Q/\Delta\phi \times p$. As discussed in Section II-B, the energy consumption associated with this charge transport is dictated by the power dissipation in a series resistor R_i during charging and discharging the capacitance $C = Q/U$ of the modulator. This energy dissipation is independent of the exact value of R_i and, for a single charging process, can be estimated to be $W = QU/2$ [35]. We may hence estimate the energy dissipation W_π, 1 dB associated with a phase shift of π in a device having a 1 dB insertion loss,

$$W_{\pi,1\ \mathrm{dB}} = \frac{1}{2} \times \frac{\Delta Q}{\Delta\Phi}\pi \times \frac{aU_\pi L}{1\ \mathrm{dB}}. \tag{8}$$

This FOMis indicated in the last column of Table I. The best power efficiency is obtained using SOH devices. POH devices require the smallest charge transport to achieve a π phase shift, but they suffer from high propagation losses and hence need to be kept short. This leads to higher operation voltages and hence to a higher energy consumption. Still, POH devices have distinct advantages when it comes to device footprint, enabling modulator lengths of only several tens of micrometers. Moreover, the superior modulation bandwidth of POH devices makes them particularly well suited for applications in THz EO modulation and signal processing. Note that the numbers given here for POH modulators were obtained from first proof-of-concept experiments, whereas pn-depletion-type devices have been optimized over many years.

V. SUMMARY AND OUTLOOK

We have given an overview on recent progress in SOH and POH integration. The concepts combine highly efficient organic EO materials with silicon photonic and plasmonic waveguides. This enables highly efficient modulators with unprecedented performance and compactness. Experimental demonstrations of SOH devices include low-power operation at an energy consumption of a few femtojoule per bit, ultra-fast modulation at frequencies of up to 100 GHz, as well as IQ signaling using advanced modulation formats such as QPSK and 16QAM. POH modulators stand out due to an ultra-compact footprint and due to the absence of practically relevant intrinsic speed limitations.

Current research in the field of SOH EO modulators aims at further increasing the device performance. We have recently demonstrated that SOH devices do not only support 100 Gb/s on-off-keying (OOK) [52], but also 4ASK signaling at symbol rates of 64 GBd—both at room temperature and at 80 C [49]. Beyond these experiments, there is still a series of practical device-related aspects that need systematic investigation in both SOH and POH modulators. As an example, drift of the operating point, which is well known and thoroughly investigated in LiNbO_3 [53] and other devices with insulating EO layer, is also observed in SOH and POH devices and requires further investigation.

Another branch of research concentrates on improved organic EO materials. Currently, in most material systems, less than 15% of the EO activity inherent in the chromophores is translated to macroscopic EO effects by poling, and the poling efficiency depends on the poling configuration. Improved quantum and statistical mechanical (multiscale) theoretical methods [54]–[59] have led to new classes of organic EO materials and to systematic improvements of the poling efficiency, enabling macroscopic EO coefficients r_{33} in excess of 500 pm/V in thin films [54], [55]. Theoretical calculations also suggest that new chromophores with significantly improved molecular first-order hyperpolarizability are possible [54], which may even lead to EO coefficients r_{33} in excess of 1000 pm/V, thereby enabling SOH modulators with π-voltages of less than 100 mV. Moreover, theoretical guidance has also helped to reduce optical loss through control of the homogeneity of the material refractive index.

Besides improving of EO coefficients, systematic investigation and optimization of thermal and photochemical stability of EO cladding materials is subject of ongoing research. Thermal stability is defined by lattice hardness and usually quantified by the glass transition temperature T_g of the material [55]. A glass transition temperature of $T_g = 150$ C is adequate to satisfy Telcordia standards, and such temperatures are easily achieved by crosslinking chemistry, for which values of $T_g = 200$ C are routinely obtained [55]. A specific advantage of organic EO materials is that a variety of parameters such as EO activity, optical loss, dielectric permittivity, lattice hardness, material compatibility, and material processability can be simultaneously optimized by systematic chemical modification and by molecular engineering of the material. We believe that focused material-related research activities in the future will help to unlock the full potential of theory-guided design and synthesis of functional materials for both SOH and POH devices.

APPENDIX
CHARGE TRANSFER IN OPTICAL PHASE SHIFTERS

SOH and POH EO devices show superior efficiency in comparison to conventional silicon photonic modulators based on FCD. To quantify this advantage, we consider first a conventional phase shifter based on an SOI strip waveguide of width w and height h, which exploits refractive index changes in the silicon waveguide core due to modulation of the free-carrier density, see Fig. 9(a) for an illustration of the waveguide cross section. For the analysis, we use a time and space dependence of the form $\exp(j\omega t - j\beta z)$, where $\omega = 2\pi c/l$ denotes the angular frequency of light with a vacuum wavelength λ, while β is the modal propagation constant along the propagation direction z. The phase shift $\Delta\varphi$ accumulated along a waveguide of length L can then be calculated to be

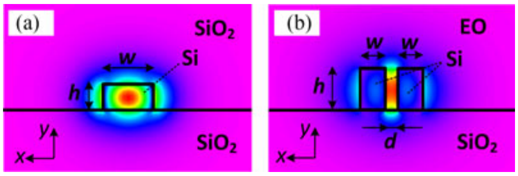

Fig. 9. Schematic cross section of silicon photonic phase shifters. (a) Conventional phase shifter, exploiting refractive index changes due to FCD in the silicon (Si) waveguide core. (b) Slot-waveguide SOH phase shifter, exploiting the refractive index change in the organic EO cladding. In both structures, electric contacts have been omitted for simplicity.

$$\Delta\Phi = -k_0 \Delta n_{\mathrm{e}} L, \quad k_0 = \frac{2\pi}{\lambda}. \tag{9}$$

In this relation, Δn_e denotes the change of the effective refractive index $n_e = \beta/k_0$ of the waveguide mode as a consequence of free-carrier injection or depletion. In silicon, the carrier-induced refractive index change is dominated by the contribution of holes and can be approximated by

$$\delta n_{\mathrm{Si}} = -8.36 \times 10^{-18} \mathrm{cm}^{2.4} \times N_h^{0.8} \tag{10}$$

where N_h denotes the density of holes [60]. The exponent of 0.8 makes the relationship of Eq. (10) slightly nonlinear, but we may use a linear approximation which is valid in the vicinity of a typical reference hole densities of $N_{\mathrm{h0}} = 10^{17}$ cm^{-3},

$$\Delta n_{\mathrm{Si}} = -B \times \Delta N_h \tag{11}$$

where $\Delta N_h = N_h - N_{\mathrm{h0}}$ denotes the deviation of the hole density from the reference hole density N_{h0}, and where $\Delta n_{\mathrm{Si}} = \delta n_{\mathrm{Si}}(N_h) - \delta n_{\mathrm{Si}}(N_{\mathrm{h0}})$is the corresponding refractive index change. The quantity $B = 2.7 \times 10^{-21} \mathrm{cm}^3$ is a constant that relates the change of the hole density in silicon to the change of the refractive index. Within the SOI waveguide, both the change of the hole density $\Delta N_h(x,y)$ and the refractive index change $\Delta n_{\mathrm{Si}}(x,y)$depend on the lateral coordinates x and y, and the corresponding change of the effective refractive index must hence be evaluated by an overlap integral in terms of the vectorial modal fields $\underline{\mathcal{E}}_0(x,y)$ and $\underline{\mathcal{H}}_0(x,y)$ of the fundamental waveguide mode [61],

$$\Delta n_{\mathrm{e}} = \frac{c\varepsilon_0 n_{\mathrm{Si}} \iint_{-\infty}^{\infty} \Delta n_{\mathrm{Si}}(x,y) \left|\underline{\mathcal{E}}_0(x,y)\right|^2 \mathrm{d}x\mathrm{d}y}{\iint_{-\infty}^{\infty} \mathrm{Re}\left\{\underline{\mathcal{E}}_0(x,y) \times \underline{\mathcal{H}}_0^*(x,y)\right\} \cdot \mathbf{e}_z \mathrm{d}x\mathrm{d}y}. \tag{12}$$

In this relation, $n_{\mathrm{Si}} \approx 3.48$ is the refractive index of the silicon core at the reference hole density of $N_{\mathrm{h0}} = 10^{17}$ cm^{-3}. Eq. (12) indicates that the performance of conventional silicon-based phase shifters can be optimized by designing the waveguide such that the hole density changes $\Delta N_h(x,y)$ and the associated refractive variations $\Delta n_{\mathrm{Si}}(x,y)$ occur in a region where the modal field $\underline{\mathcal{E}}_0(x,y)$ is strong [9].

For a coarse estimation of the device efficiency, we may neglect this effect and simplify Eq. (12) by assuming that holes are injected or depleted homogeneously in the cross section of the waveguide core. As a consequence, both $\Delta N_h\,(x,y)$ and $\Delta n_{\mathrm{Si}}\,(x,y)$ assume constant values of $\Delta N_{h,\mathrm{core}}$ and $\Delta n_{\mathrm{Si,core}}$ within the waveguide core and are zero in the cladding. Note that this is equivalent to assuming that the square of the mode field magnitude $|\underline{\mathcal{E}}_0\,(x,y)|^2$ can be approximated by a constant corresponding to its average value within the waveguide core. It is then irrelevant how injected or depleted holes are distributed over the cross section of the core; only the total number of transferred holes matters. Eq. (12) can then be approximated by the relation

$$\Delta n_{\mathrm{e}} = \Gamma_{\mathrm{core}} \Delta n_{\mathrm{Si,core}} \tag{13}$$

where Γ_{core} denotes the field interaction factor of the guided mode with the silicon waveguide core,

$$\Gamma_{\mathrm{core}} = \frac{c\varepsilon_0 n_{\mathrm{Si}} \iint_{D_{\mathrm{core}}} |\underline{\mathcal{E}}_0(x,y)|^2 \mathrm{d}x\mathrm{d}y}{\iint_{-\infty}^{\infty} \mathrm{Re}\left\{\underline{\mathcal{E}}_0\,(x,y) \times \underline{\mathcal{H}}_0^*\,(x,y)\right\} \cdot \mathbf{e}_z \mathrm{d}x\mathrm{d}y}. \tag{14}$$

In this relation, the integration domain D_{core} of the area integral in the numerator extends over the silicon waveguide core only. Combining Eqs. (9), (11), and (13), the phase shift can be related to the charge ΔQ of the injected holes,

$$\Delta\Phi_{\mathrm{FCD}} = \Gamma_{\mathrm{core}} k_0 \frac{B\,\Delta Q_{\mathrm{FCD}}}{\mathrm{ewh}} \tag{15}$$

where the charge ΔQ_{FCD} is obtained from the elementary charge $e = 1.602 \times 10^{-19}$ C multiplied by the total number of holes within the volume $V = whL$ of the waveguide core,

$$\Delta Q_{\mathrm{FCD}} = e\,w\,h\,L\,\Delta N_h. \tag{16}$$

Solving Eqs. (15) and (16) for the ratio $\Delta Q_{\mathrm{FCD}}/\Delta\phi_{\mathrm{FCD}}$ leads to Eq. (3) of the main text.

Similarly, we can estimate the phase-shift related charge transfer in SOH devices. To this end let us consider a slot waveguide of length *L* having a cross section as depicted in Fig. 9 (b) with a voltage *U* applied between the two silicon rails. The phase shift $\Delta\varphi$ accumulated along the waveguide is again calculated according to Eq. (9), where the change Δn_e of the effective refractive index of the mode can be approximated by an overlap integral of the mode field with the local index change $\Delta n_{\mathrm{EO}}\,(x,y)$ of the EO cladding [61],

$$\Delta n_{\mathrm{e}} = \frac{c\varepsilon_0 n_{\mathrm{EO}} \iint_{-\infty}^{\infty} \Delta n_{\mathrm{EO}}\,(x,y)\,\left|\underline{\mathcal{E}}_{0,x}\,(x,y)\right|^2 \mathrm{d}x\mathrm{d}y}{\iint_{-\infty}^{\infty} \mathrm{Re}\left\{\underline{\mathcal{E}}_0\,(x,y) \times \underline{\mathcal{H}}_0^*\,(x,y)\right\} \cdot \mathbf{e}_z \mathrm{d}x\mathrm{d}y}. \tag{17}$$

In this relation, n_{EO} denotes the refractive index of the EO cladding seen by the dominant electric field component $\mathcal{E}_x$ of the optical quasi-TE mode without any voltage applied to the device. Similarly, $\Delta n_{\mathrm{EO}}(x,y)$ denotes the local voltage-induced change of the refractive index that affects the optical $\mathcal{E}_x$-component. The overlap integral in the numerator of Eq. (17) contains only the *x*-component $\underline{\mathcal{E}}_{0,x}\,(x,y)$ of the vectorial electric mode field $\underline{\mathcal{E}}_0\,(x,y)$. For simplicity, we may assume that the modulating RF field features only an *x*-component which assumes a constant value of $E_{\mathrm{mod},x} = U/d$ in the slot region D_{slot} and which is negligible outside. Here, D_{slot} denotes a rectangular region having the width and the height of the slot, see Fig. 8(b) and (c). Using these assumptions, the refractive index change of the cladding can be assumed to have a constant value of $\Delta n_{\mathrm{EO,slot}}$ in the slot and to be zero elsewhere, where

$$\Delta n_{\mathrm{EO,slot}} = -\frac{1}{2} n_{\mathrm{EO}}^3 r_{33} \frac{U}{d}. \tag{18}$$

In this relation, the quantity r_{33} denotes the EO coefficient of the cladding for electric fields oriented in parallel to the material's active optical axis, which is aligned along the *x*-direction of the waveguide coordinate system. The associated change of the effective mode index can now be estimated by multiplying the refractive index change $\Delta n_{\mathrm{EO,slot}}$ in the slot with the field interaction factor $\Gamma_{\mathrm{slot,x}}$ of the mode with the slot region D_{slot},

$$\Delta n_{\mathrm{e}} = \Gamma_{\mathrm{slot,x}} \Delta n_{\mathrm{EO,slot}} \tag{19}$$

where

$$\Gamma_{\mathrm{slot,x}} = \frac{c\varepsilon_0 n_{\mathrm{EO}} \iint_{D\mathrm{slot}} |\underline{\mathcal{E}}_{0,x}(x,y)|^2 \mathrm{d}x\mathrm{d}y}{\iint_{-\infty}^{\infty} \mathrm{Re}\left\{\underline{\mathcal{E}}_0\,(x,y) \times \underline{\mathcal{H}}_0^*\,(x,y)\right\} \cdot \mathbf{e}_z \mathrm{d}x\mathrm{d}y}. \tag{20}$$

In this relation, the area integral in the numerator extends only over the slot region D_{slot}. Note that Eq. (20) can also be applied to POH devices, where it accounts also for effects of reduced group velocity of the plasmonic slot waveguide mode.

The charge transfer associated with applying a voltage *U* to the slot waveguide can be estimated by approximating the slot waveguide by a parallel-plate capacitor filled with the EO polymer of relative permittivity ε_r. The associated capacitance amounts to $C = \varepsilon_0 \varepsilon_r hL/d$, leading to a charge transfer of

$$\Delta Q_{\mathrm{SOH}} = \varepsilon_0 \varepsilon_r \frac{hL}{d} U. \tag{21}$$

Combining Eqs. (9), (18), (19), and (21), the phase shift can be related to the charge ΔQ of the injected holes,

$$\Delta\Phi_{\mathrm{SOH}} = \Gamma_{\mathrm{slot,x}} k_0 \frac{r_{33} n_{\mathrm{EO}}^3\,\Delta Q_{\mathrm{SOH}}}{\varepsilon_0 \varepsilon_r h}. \tag{22}$$

Solving Eq. (22) for the ratio $\Delta Q_{\mathrm{SOH}}/\Delta\phi_{\mathrm{SOH}}$ leads to Eq. (4) of the main text. Note that the derivation of Eq. (22) is independent from the material of the waveguide rails through which the voltage is applied to the EO material. All relations obtained for SOH phase shifters can hence be directly transferred to POH devices.

REFERENCES

[1] J. S. Orcutt, B. Moss, C. Sun, J. Leu, M. Georgas, J. Shainline, E. Zgraggen, H. Li, J. Sun, M. Weaver, S. Urošević, M. Popović, R. J. Ram, and V. Stojanović, "Open foundry platform for high-performance electronic-photonic integration," *Opt. Exp.*, vol. 20, no. 11, pp. 12222–12232, 2012.

[2] G. T. Reed, G. Mashanovich, F. Y. Gardes, and D. J. Thomson, "Silicon optical modulators," *Nature Photon.*, vol. 4, no. 8, pp. 518–526, 2010.

[3] P. Dong, X. Liu, S. Chandrasekhar, L. L. Buhl, R. Aroca, and Y.-K. Chen, "Monolithic silicon photonic integrated circuits for compact 100+ Gb/s coherent optical receivers and transmitters," *IEEE J. Sel. Topics Quantum Electron.*, vol. 20, no. 4, pp. 150–157, Jul./Aug. 2014.

[4] P. Dong, C. Xie, L. Chen, L. L. Buhl, and Y.-K. Chen, "112-Gb/s monolithic PDM-QPSK modulator in silicon," *Opt. Exp.*, vol. 20, no. 26, pp. B624–B629, 2012.

[5] D. J. Thomson, F. Y. Gardes, Y. Hu, G. Mashanovich, M. Fournier, P. Grosse, J.-M. Fedeli, and G. T. Reed, "High contrast 40Gbit/s optical modulation in silicon," *Opt. Exp.*, vol. 19, no. 12, pp. 11507–11516, 2011.

[6] W. M. Green, M. J. Rooks, L. Sekaric, and Y. A. Vlasov, "Ultra-compact, low RF power, 10 Gb/s silicon Mach–Zehnder modulator," *Opt. Exp.*, vol. 15, no. 25, pp. 17106–17113, 2007.

[7] J. Fujikata, J. Ushida, Y. Ming-Bin, Z. ShiYang, D. Liang, P. Lo Guo-Qiang, D.-L. Kwong, and T. Nakamura, "25 GHz operation of silicon optical modulator with projection MOS structure," presented at the Optical Fiber Communication Conf./Nat. Fiber Optical Engineering Conf., San Diego, CA, USA, 2010, Paper OMI3.

[8] H. Xu, X. Li, X. Xiao, P. Zhou, Z. Li, J. Yu, and Y. Yu, "High-speed silicon modulator with band equalization," *Opt. Lett.*, vol. 39, no. 16, pp. 4839–4842, 2014.

[9] M. R. Watts, W. A. Zortman, D. C. Trotter, R. W. Young, and A. L. Lentine, "Low-voltage, compact, depletion-mode, silicon Mach–Zehnder modulator," *IEEE J. Sel. Topics Quantum Electron.*, vol. 16, no. 1, pp. 159–164, Jan./Feb. 2010.

[10] J. A. Dionne, K. Diest, L. A. Sweatlock, and H. A. Atwater, "PlasMOStor: A metal-oxide-Si field effect plasmonic modulator," *Nano Lett.*, vol. 9, no. 2, pp. 897–902, 2009.

[11] A. Melikyan, N. Lindenmann, S. Walheim, P. M. Leufke, S. Ulrich, J. Ye, P. Vincze, H. Hahn, T. Schimmel, C. Koos, W. Freude, and J. Leuthold, "Surface plasmon polariton absorption modulator," *Opt. Exp.*, vol. 19, no. 9, pp. 8855–8869, 2011.

[12] V. J. Sorger, N. D. Lanzillotti-Kimura, R.-M. Ma, and X. Zhang, "Ultra-compact silicon nanophotonic modulator with broadband response," *Nanophoton.*, vol. 1, no. 1, pp. 17–22, 2012.

[13] E. Feigenbaum, K. Diest, and H. A. Atwater, "Unity-order index change in transparent conducting oxides at visible frequencies," *Nano Lett.*, vol. 10, no. 6, pp. 2111–2116, 2010.

[14] J. Leuthold, C. Koos, W. Freude, L. Alloatti, R. Palmer, D. Korn, J. Pfeifle, M. Lauermann, R. Dinu, S. Wehrli, M. Jazbinsek, P. Gunter, M. Waldow, T. Wahlbrink, J. Bolten, H. Kurz, M. Fournier, J.-M. Fedeli, H. Yu, and W. Bogaerts, "Silicon-organic hybrid electro-optical devices," *IEEE J. Sel. Topics Quantum Electron.*, vol. 19, no. 6, pp. 114–126, Nov./Dec. 2013.

[15] C. Koos, J. Leuthold, W. Freude, M. Kohl, L. Dalton, W. Bogaerts, A. L. Giesecke, M. Lauermann, A. Melikyan, S. Koeber, S. Wolf, C. Weimann, S. Muehlbrandt, K. Koehnle, J. Pfeifle, R. Palmer, L. Alloatti, D. Elder, T. Wahlbrink, and J. Bolten, "Silicon-organic hybrid (SOH) and plasmonic-organic hybrid (POH) integration," presented at the Optical Fiber Communication Conf., Los Angeles, CA, USA, 2015, Paper Tu2A.1.

[16] C. Koos, J. Leuthold, W. Freude, L. Dalton, S. Koeber, R. Palmer, C. Weimann, D. Elder, W. Heni, D. Korn, J. Pfeifle, S. Wolf, D. Bekele, M. Woessner, L. Alloatti, P. Schindler, and S. Koenig, "Femtojoule modulation and frequency comb generation in silicon-organic hybrid (SOH) devices," presented at the 16th Int. Conf. Trans. Optical Networks, Graz, Austria, 6–10, Jul. 2014, Paper We.C2.1.

[17] R. Palmer, L. Alloatti, D. Korn, P. C. Schindler, R. Schmogrow, W. Heni, S. Koenig, J. Bolten, T. Wahlbrink, M. Waldow, H. Yu, W. Bogaerts, P. Verheyen, G. Lepage, M. Pantouvaki, J. van Campenhout, P. Absil, R. Dinu, W. Freude, C. Koos, and J. Leuthold, "Silicon-organic hybrid MZI modulator generating OOK, BPSK and 8-ASK signals for up to 84 Gbit/s," *IEEE Photon. J.*, vol. 5, no. 2, p. 6600907, Apr. 2013.

[18] C. Weimann, P. C. Schindler, R. Palmer, S. Wolf, D. Bekele, D. Korn, J. Pfeifle, S. Koeber, R. Schmogrow, L. Alloatti, D. Elder, H. Yu, W. Bogaerts, L. R. Dalton, W. Freude, J. Leuthold, and C. Koos, "Silicon-organic hybrid (SOH) frequency comb sources for terabit/s data transmission," *Opt. Exp.*, vol. 22, no. 3, pp. 3629–3637, 2014.

[19] R. Palmer, S. Koeber, D. L. Elder, M. Woessner, W. Heni, D. Korn, M. Lauermann, W. Bogaerts, L. Dalton, W. Freude, J. Leuthold, and C. Koos, "High-speed, low drive-voltage silicon-organic hybrid modulator based on a binary-chromophore electro-optic material," *J. Lightw. Technol.*, vol. 32, no. 16, pp. 2726–2734, Aug. 2014.

[20] S. Koeber, R. Palmer, M. Lauermann, W. Heni, D. L. Elder, D. Korn, M. Woessner, L. Alloatti, S. Koenig, P. C. Schindler, H. Yu, W. Bogaerts, L. R. Dalton, W. Freude, J. Leuthold, and C. Koos, "Femtojoule electro-optic modulation using a silicon–organic hybrid device," *Light Sci. Appl.*, vol. 4, no. 2, p. e255, 2015.

[21] L. Alloatti, R. Palmer, S. Diebold, K. P. Pahl, B. Chen, R. Dinu, M. Fournier, J.-M. Fedeli, T. Zwick, W. Freude, C. Koos, and J. Leuthold, "100 GHz silicon-organic hybrid modulator," *Light Sci. Appl.*, vol. 3, no. 5, p. e173, 2014.

[22] M. Lauermann, R. Palmer, S. Koeber, P. C. Schindler, D. Korn, T. Wahlbrink, J. Bolten, M. Waldow, D. L. Elder, L. R. Dalton, J. Leuthold, W. Freude, and C. Koos, "Low-power silicon-organic hybrid (SOH) modulators for advanced modulation formats," *Opt. Exp.*, vol. 22, no. 24, pp. 29927–29936, 2014.

[23] M. Lauermann, S. Wolf, P. C. Schindler, R. Palmer, S. Koeber, D. Korn, L. Alloatti, T. Wahlbrink, J. Bolten, M. Waldow, M. Koenigsmann, M. Kohler, D. Malsam, D. L. Elder, P. V. Johnston, N. Phillips-Sylvain, P. A. Sullivan, L. R. Dalton, J. Leuthold, W. Freude, and C. Koos, "40 GBd 16QAM signaling at 160 Gb/s in a silicon-organic hybrid modulator," *J. Lightw. Technol.*, vol. 33, no. 6, pp. 1210–1216, Mar. 2015.

[24] S. Wolf, M. Lauermann, P. Schindler, G. Ronniger, K. Geistert, R. Palmer, S. Köber, W. Bogaerts, J. Leuthold, W. Freude, and C. Koos, "DAC-less amplifier-less generation and transmission of QAM signals using sub-volt silicon-organic hybrid modulators," *J. Lightw. Technol.*, vol. 33, no. 7, pp. 1425–1432, Apr. 2015.

[25] A. Melikyan, L. Alloatti, A. Muslija, D. Hillerkuss, P. C. Schindler, J. Li, R. Palmer, D. Korn, S. Muehlbrandt, D. van Thourhout, B. Chen, R. Dinu, M. Sommer, C. Koos, M. Kohl, W. Freude, and J. Leuthold, "High-speed plasmonic phase modulators," *Nature Photon.*, vol. 8, no. 3, pp. 229–233, 2014.

[26] A. Melikyan, K. Koehnle, M. Lauermann, R. Palmer, S. Koeber, S. Muehlbrandt, P. C. Schindler, D. L. Elder, S. Wolf, W. Heni, C. Haffner, Y. Fedoryshyn, D. Hillerkuss, M. Sommer, L. R. Dalton, D. van Thourhout, W. Freude, M. Kohl, J. Leuthold, and C. Koos, "Plasmonic-organic hybrid (POH) modulators for OOK and BPSK signaling at 40 Gbit/s," *Opt. Exp.*, vol. 23, no. 8, pp. 9938–9946, 2015.

[27] C. Haffner, W. Heni, Y. Fedoryshyn, J. Niegemann, A. Melikyan, D. L. Elder, B. Baeuerle, Y. Salamin, A. Josten, U. Koch, C. Hoessbacher, F. Ducry, L. Juchli, A. Emboras, D. Hillerkuss, M. Kohl, L. R. Dalton, C. Hafner, and J. Leuthold, "All-plasmonic Mach–Zehnder modulator enabling optical high-speed communication at the microscale," *Nature Photon.*, vol. 9, pp. 525–528 2015.

[28] W. Heni, A. Melikyan, C. Haffner, Y. Fedoryshyn, B. Baeuerle, A. Josten, J. Niegemann, D. Hillerkuss, M. Kohl, D. Elder, L. Dalton, C. Hafner, and J. Leuthold, "Plasmonic Mach–Zehnder modulator with >70 GHz electrical bandwidth demonstrating 90 Gbit/s 4-ASK," presented at the Optical Fiber Communication Conf., Los Angeles, CA, USA, 2015, Paper Tu2A.2.

[29] V. R. Almeida, Q. Xu, C. A. Barrios, and M. Lipson, "Guiding and confining light in void nanostructure," *Opt. Lett.*, vol. 29, no. 11, pp. 1209–1211, 2004.

[30] R. Palmer, L. Alloatti, D. Korn, W. Heni, P. C. Schindler, J. Bolten, M. Karl, M. Waldow, T. Wahlbrink, W. Freude, C. Koos, and J. Leuthold, "Low-loss silicon strip-to-slot mode converters," *IEEE Photon. J.*, vol. 5, no. 1, p. 2200409, Feb. 2013.

[31] L. Alloatti, M. Lauermann, C. Sürgers, C. Koos, W. Freude, and J. Leuthold, "Optical absorption in silicon layers in the presence of charge inversion/accumulation or ion implantation," *Appl. Phys. Lett.*, vol. 103, no. 5, p. 051104, 2013.

[32] J. Pfeifle, L. Alloatti, W. Freude, J. Leuthold, and C. Koos, "Silicon-organic hybrid phase shifter based on a slot waveguide with a liquid-crystal cladding," *Opt. Exp.*, vol. 20, no. 14, pp. 15359–15376, 2012.

[33] Y. Xing, T. Ako, J. George, D. Korn, H. Yu, P. Verheyen, M. Pantouvaki, G. Lepage, P. Absil, A. Ruocco, C. Koos, J. Leuthold, K. Neyts, J. Beeckman, W. Bogaerts, "Digitally controlled phase shifter using an SOI slot waveguide with liquid crystal infiltration," *IEEE Photon. Technol. Lett.*, vol. 27, no. 12, pp. 1269–1272, Jun. 2015.

[34] D. Korn, M. Lauermann, P. Appel, L. Alloatti, R. Palmer, W. Freude, J. Leuthold, and C. Koos, "First silicon-organic hybrid laser at telecommunication wavelength," presented at the Conf. Lasers Electro-Optics, San Jose, CA, USA, 2012, Paper CTu2I.1.

[35] D. A. B. Miller, "Energy consumption in optical modulators for interconnects," *Opt. Exp.*, vol. 20, no. 102, pp. A293–A308, 2012.

[36] L. Alloatti, D. Korn, R. Palmer, D. Hillerkuss, J. Li, A. Barklund, R. Dinu, J. Wieland, M. Fournier, J. Fedeli, H. Yu, W. Bogaerts, P. Dumon, R. Baets, C. Koos, W. Freude, and J. Leuthold, "42.7 Gbit/s electro-optic modulator in silicon technology," *Opt. Exp.*, vol. 19, no. 12, pp. 11841–11851, 2011.

[37] R. Ding, T. Baehr-Jones, Y. Liu, R. Bojko, J. Witzens, S. Huang, J. Luo, S. Benight, P. Sullivan, J.-M. Fedeli, M. Fournier, L. Dalton, A. Jen, and M. Hochberg, "Demonstration of a low V pi L modulator with GHz bandwidth based on electro-optic polymer-clad silicon slot waveguides," *Opt. Exp.*, vol. 18, no. 15, pp. 15618–15623, 2010.

[38] D. L. Elder, S. J. Benight, J. Song, B. H. Robinson, and L. R. Dalton, "Matrix-assisted poling of monolithic bridge-disubstituted organic NLO chromophores," *Chem. Mater.*, vol. 26, no. 2, pp. 872–874, 2014.

[39] Y. Jouane, Y-C. Chang, D. Zhang, J. Luo, A. K-Y. Jen, and Y. Enami, "Unprecedented highest electro-optic coefficient of 226 pm/V for electro-optic polymer/TiO2 multilayer slot waveguide modulators," *Opt. Exp.*, vol. 22, no. 22, pp. 27725–27732, 2014.

[40] J. Takayesu, M. Hochberg, T. Baehr-Jones, E. Chan, G. Wang, P. Sullivan, Y. Liao, J. Davies, L. Dalton, A. Scherer, and W. Krug, "A hybrid electrooptic microring resonator-based $1\times4\times1$ ROADM for wafer scale optical interconnects," *J. Lightw. Technol.*, vol. 27, no. 4, pp. 440–448, Feb. 2009.

[41] P. A. Sullivan and L. R. Dalton, "Theory-inspired development of organic electro-optic materials," *Acc. Chem. Res.*, vol. 43, no. 1, pp. 10–18, 2010.

[42] L. R. Dalton, D. Lao, B. C. Olbricht, S. Benight, D. H. Bale, J. A. Davies, T. Ewy, S. R. Hammond, and P. A. Sullivan, "Theory-inspired development of new nonlinear optical materials and their integration into silicon photonic circuits and devices," *Opt. Mater.*, vol. 32, no. 6, pp. 658–668, 2010.

[43] L. R. Dalton, P. A. Sullivan, and D. H. Bale, "Electric field poled organic electro-optic materials: State of the art and future prospects," *Chem. Rev.*, vol. 110, no. 1, pp. 25–55, 2010.

[44] R. Palmer, L. Alloatti, D. Korn, P. C. Schindler, M. Baier, J. Bolten, T. Wahlbrink, M. Waldow, R. Dinu, W. Freude, C. Koos, and J. Leuthold, "Low power Mach–Zehnder modulator in silicon-organic hybrid technology," *IEEE Photon. Technol. Lett.*, vol. 25, no. 13, pp. 1226–1229, Jul. 2013.

[45] Y. V. Pereverzev, K. N. Gunnerson, O. V. Prezhdo, P. A. Sullivan, Y. Liao, B. C. Olbricht, A. J. P. Akelaitis, A. K.-Y. Jen, and L. R. Dalton, "Guest−host cooperativity in organic materials greatly enhances the nonlinear optical response," *J. Phys. Chem. C*, vol. 112, no. 11, pp. 4355–4363, 2008.

[46] Y. Enami, C. T. Derose, D. Mathine, C. Loychik, C. Greenlee, R. A. Norwood, T. D. Kim, J. Luo, Y. Tian, A. K.-Y. Jen, and N. Peyghambarian, "Hybrid polymer/sol–gel waveguide modulators with exceptionally large electro–optic coefficients," *Nature Photon.*, vol. 1, no. 3, pp. 180–185, 2007.

[47] F. Chang, K. Onohara, and T. Mizuochi, "Forward error correction for 100 G transport networks," *IEEE Commun. Mag.*, vol. 48, no. 3, pp. S48–S55, Mar. 2010.

[48] T. Baehr-Jones, R. Ding, Y. Liu, A. Ayazi, T. Pinguet, N. C. Harris, M. Streshinsky, P. Lee, Y. Zhang, A. E.-J. Lim, T.-Y. Liow, S. H.-G. Teo, G.-Q. Lo, and M. Hochberg, "Ultralow drive voltage silicon traveling-wave modulator," *Opt. Exp.*, vol. 20, no. 11, pp. 12014–12020, 2012.

[49] M. Lauermann, S. Wolf, R. Palmer, A. Bielik, L. Altenhain, J. Lutz, R. Schmid, T. Wahlbrink, J. Bolten, A. L. Giesecke, W. Freude, and C. Koos, "64 GBd operation of a silicon-organic hybrid modulator at elevated temperature," presented at the Optical Fiber Communication Conf., Los Angeles, CA, USA, 2015, Paper Tu2A.5.

[50] S. Wolf, P. C. Schindler, G. Ronniger, M. Lauermann, R. Palmer, S. Koeber, D. Korn, W. Bogaerts, J. Leuthold, W. Freude, and C. Koos, "10 GBd SOH modulator directly driven by an FPGA without electrical amplification," presented at the 40th European Conf. Optical Communication, Cannes, France, 2014, Paper Mo.4.5.4.

[51] R. Ding, T. Baehr-Jones, W.-J. Kim, B. Boyko, R. Bojko, A. Spott, A. Pomerene, C. Hill, W. Reinhardt, and M. Hochberg, "Low-loss asymmetric strip-loaded slot waveguides in silicon-on-insulator," *Appl. Phys. Lett.*, vol. 98, no. 23, p. 233303, 2011.

[52] W. Hartmann, M. Lauermann, S. Wolf, H. Zwickel, Y. Kutuvantavida, J. Luo, A. K.-Y. Jen, W. Freude, and C. Koos, "100 Gbit/s OOK using a silicon-organic hybrid (SOH) modulator," presented at the 41th European Conf. Optical Communication, Valencia, Spain, 2015, Paper PDP 1.4.

[53] J. P. Salvestrini, L. Guilbert, M. Fontana, M. Abarkanm, and S. Gille, "Analysis and control of the DC drift in LiNbO$_3$-based Mach–Zehnder modulators," *J. Lightw. Technol.*, vol. 29, no. 10, pp. 1522–1534, May 2011.

[54] W. Jin, P. V. Johnston, D. L. Elder, A. F. Tillack, B. C. Olbricht, J. Song, P. J. Reid, R. Xu, B. H. Robinson, and L. R. Dalton, "Benzocyclobutene barrier layer for suppressing conductance in nonlinear optical devices during electric-field poling," *Appl. Phys. Lett.*, vol. 104, pp. 243304–1–243304-3, 2014.

[55] L. R. Dalton, M. Jazbinsek, O. P. Kwon, P. Guenter, and P. A. Sullivan, in *Organic Electro-Optics and Photonics*. Cambridge, U.K.: Cambridge Univ. Press, 2015, pp. 1–293.

[56] A. F. Tillack, "Electro-optic material design criteria derived from condensed matter simulations using the level-of-detail coarse-graining approach," Ph.D. dissertation, Univ. Washington, Seattle,WA, USA, 2015.

[57] L. E. Johnson, L. R. Dalton, and B. H. Robinson, "Optimizing calculations of electronic excitations and relative hyperpolarizabilities of electrooptic chromophores," *Acc. Chem. Res.*, vol. 47, no. 11, pp. 3258–3265, 2014.

[58] P. A. Sullivan and L. R. Dalton, "The materials genome for organic electro-optics and silicon/plasmonic—organic hybrid technology," in *New Horizons in Nanoscience and Engineering*, D. L. Andrews and J. G. Grote, Eds. Bellingham, WA, USA: SPIE Press, pp. 233–284, 2015.

[59] L. R. Dalton, M. Lauermann, and C. Koos, "Nonlinear optics: Electro-optic applications," in *The WSPC Reference on Organic Electronics: Organic Semiconductors*, vol. 7, J.-L. Bredas and S. R. Marder, Eds. Singapore and London: World Scientific and Imperial College Press, 2015, ch. 13.

[60] R. Soref and B. Bennett, "Electrooptical effects in silicon," *IEEE J. Quantum Electron.*, vol. 23, no. 1, pp. 123–129, Jan. 1987.

[61] C. Koos, *Nanophotonic Devices Linear Nonlinear Optical Signal Processing*,. Karlsruhe, Germany: Univ.-Verl. Karlsruhe, 2007.

Authors' biographies are not available at the time of publication.

QUERIES

Q1. Author: Please check the name of all authors for correctness.

Silicon-Organic Hybrid (SOH) and Plasmonic-Organic Hybrid (POH) Integration

Christian Koos, *Member, IEEE*, Juerg Leuthold, *Fellow, IEEE*, Wolfgang Freude, *Senior Member, IEEE*, Manfred Kohl, Larry Dalton, *Senior Member, IEEE*, Wim Bogaerts, *Senior Member, IEEE*, Anna Lena Giesecke, Matthias Lauermann, Argishti Melikyan, Sebastian Koeber, Stefan Wolf, Claudius Weimann, Sascha Muehlbrandt, Kira Koehnle, Joerg Pfeifle, Wladislaw Hartmann, Yasar Kutuvantavida, Sandeep Ummethala, Robert Palmer, Dietmar Korn, Alloatti Luca, Philipp Claudius Schindler, Delwin L. Elder, Thorsten Wahlbrink, and Jens Bolten

(Invited Paper)

***Abstract*—Silicon photonics offers tremendous potential for inexpensive high-yield photonic-electronic integration. Besides conventional dielectric waveguides, plasmonic structures can also be efficiently realized on the silicon photonic platform, reducing device footprint by more than an order of magnitude. However, neither silicon nor metals exhibit appreciable second-order optical nonlinearities, thereby making efficient electro-optic modulators challenging to realize. These deficiencies can be overcome by the concepts of silicon-organic hybrid (SOH) and plasmonic-organic hybrid integration, which combine SOI waveguides and plasmonic nanostructures with organic electro-optic cladding materials.**

***Index Terms*—Electro-optic modulators, nonlinear optical devices, photonic integrated circuits, plasmonics, silicon photonics.**

I. Introduction

ELECTRO-OPTIC (EO) modulators are key building blocks for highly integrated photonic-electronic circuits on the silicon platform [1]–[4]. Due to the absence of linear EO effects in bulk silicon, current modulators mostly rely on free-carrier dispersion (FCD) by exploiting depletion [5] or injection [6] of holes in diode or metal-oxide-semiconductor (MOS) structures [7]. However, these concepts do not allow for fast devices that feature low drive voltage and small footprint simultaneously. Carrier injection enables voltage-length products as small as $U_\pi L = 0.36$ Vmm, but the free-carrier lifetime limits the modulation speed [6]. Carrier-depletion modulators, in contrast, support symbol rates of up to 70 GBd when exploiting frequency dependent impedance mismatch to compensate for the low-pass characteristic of the device [8], but typical voltage-length products are beyond 10 Vmm [2], [9]. Similarly, high-speed plasmonic modulators predominantly exploit the interaction of surface plasmon polariton (SPP) modes with free carriers in semiconductors or metals [10]–[13], thereby suffering from limitations in speed and efficiency.

These deficiencies can be overcome by the concepts of silicon-organic hybrid (SOH) and plasmonic-organic hybrid (POH) integration, which combine silicon-on-insulator (SOI) waveguides and plasmonic nanostructures with organic EO claddings. In this paper, we review recent progress in the field of SOH [14]–[24] and POH [25]–[28] integration. The SOH concept enables highly efficient modulators having voltage-length

Manuscript received July 12, 2015; revised October 14, 2015; accepted November 4, 2015. This work was supported by the European Research Council (ERC Starting Grant "EnTeraPIC," number 280145), the Alfried Krupp von Bohlen und Halbach Foundation, the EU projects PhoxTroT, BigPipes, Navolchi and SOFI, the Karlsruhe International Research School for Teratronics, the Karlsruhe School of Optics and Photonics, the Karlsruhe Nano-Micro Facility, and the Center for Functional Nanostructures of the Deutsche Forschungsgemeinschaft.

C. Koos is with the Institute of Photonics and Quantum Electronics, Institute of Microstructure Technology, Karlsruhe Institute of Technology, Karlsruhe 76131, Germany (e-mail: christian.koos@kit.edu). Q1

J. Leuthold was with the Karlsruhe Institute of Technology, Karlsruhe 76131, Germany. He is now with the Institute of Electromagnetic Fields, Swiss Federal Institute of Technology, Zürich 8092, Switzerland (e-mail: Juerg Leuthold@ethz.ch).

W. Freude, M. Lauermann, S. Wolf, C. Weimann, and J. Pfeifle are with the Institute of Photonics and Quantum Electronics, Karlsruhe Institute of Technology, Karlsruhe 76131, Germany (e-mail: w.freude@kit.edu; matthias.lauermann@kit.edu; s.wolf@kit.edu; claudi-us.weimann@kit.edu; joerg.pfeifle@kit.edu).

A. Melikyan was with the Karlsruhe Institute of Technology, Karlsruhe 76131, Germany. He is now with Alcatel-Lucent Bell Labs, Holmdel NJ 07733, USA (e-mail: argishti.melikyan@alcatel-lucent.com).

M. Kohl, S. Muehlbrandt, K. Koehnle, W. Hartmann, Y. Kutuvantavida, and S. Ummethala are with the Institute of Microstructure Technology, Karlsruhe Institute of Technology, Karlsruhe 76131, Germany (e-mail: manfred.kohl@kit.edu; sascha.muehl-brandt@kit.edu; kira.koehnle@kit.edu; wladislaw.hartmann@kit.edu; yasar.kutuvantavida@kit.edu; sandeep.ummethala@kit.edu).

L. Dalton and D. L. Elder are with the University of Washington, Seattle, WA 20052 USA (e-mail: dalton@chem.washington.edu; elderdl@uw.edu).

W. Bogaerts is with the Photonics Research Group, Ghent University—IMEC, Ghent B-9000, Belgium and also with the Luceda Photonics, Dendermonde B-9200, Belgium (e-mail: wim.bogaerts@ugent.be).

A. L. Giesecke, T. Wahlbrink, and J. Bolten are with the AMO GmbH, Aachen 52074, Germany (e-mail: giesecke@amo.de; wahlbrink@amo.de; bolten@amo.de).

S. Koeber was with the Karlsruhe Institute of Technology,, Karlsruhe 76131, Germany. He is now with Department of Chemistry, University of Cologne, Köln 50939, Germany (e-mail: sebastian.koeber@uni-koeln.de).

R. Palmer was with the Karlsruhe Institute of Technology, Karlsruhe 76131, Germany. He is now with Coriant GmbH, Munich 81541, Germany (e-mail: robert.palmer@coriant.com).

D. Korn was with the Karlsruhe Institute of Technology, Karlsruhe 76131, Germany. He is now with Imagine Optic, Orsay 91400, France (e-mail: dietmarkorn@googlemail.com).

A. Luca was with the Karlsruhe Institute of Technology, Karlsruhe 76131, Germany. He is now with Massachusetts Institute of Technology, Research Laboratory of Electronics, Cambridge, MA 02139 USA.

P. C. Schindler was with the Karlsruhe Institute of Technology, Karlsruhe 76131, Germany. He is now with Infinera Corporation, Sunnyvale, CA 94089 USA (e-mail: pschindler@infinera.com).

Color versions of one or more of the figures in this paper are available online at http://ieeexplore.ieee.org.

Digital Object Identifier 10.1109/JLT.2015.2499763

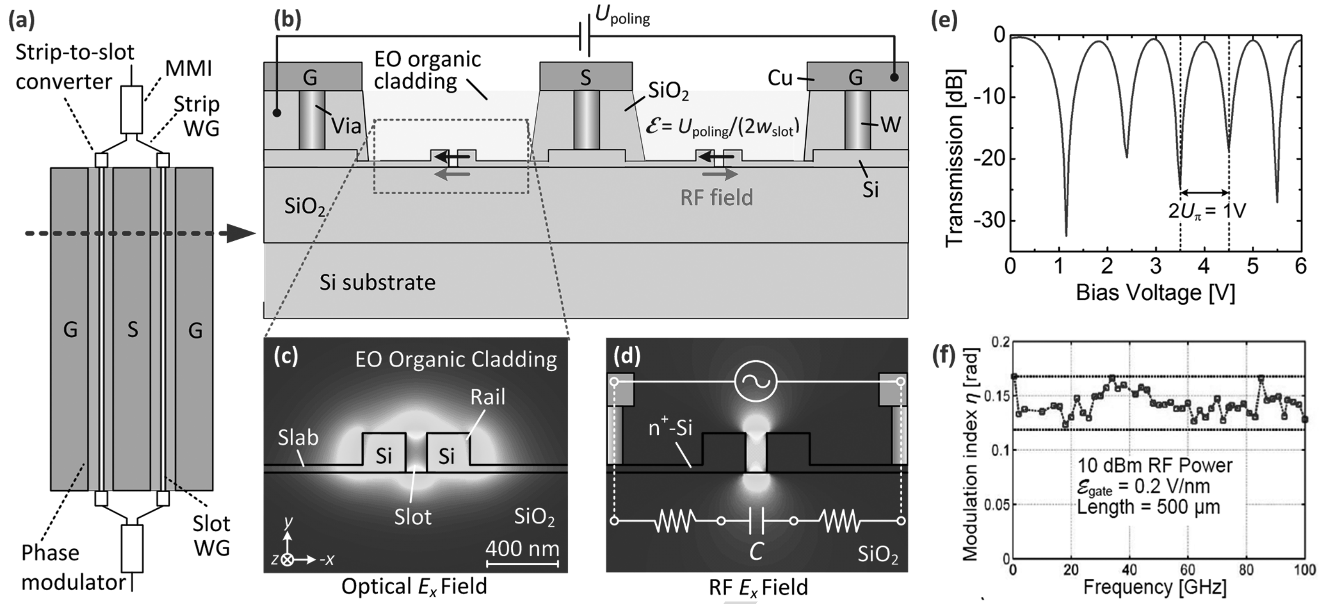

Fig. 1. Silicon-organic hybrid (SOH) MZM. (a) Schematic of the MZM. The device consists of two slot-waveguide (WG) phase modulators, driven in push-pull operation by a single coplanar GSG transmission line. Before and after the modulator sections, the light is split and combined by multimode interference couplers (MMI). (b) Cross-section of an SOH MZM using tungsten vias to connect the GSG transmission line to the Si slot waveguide. Push-pull operation is obtained by an appropriate choice of poling directions (blue arrows) of the EO cladding in both arms with respect to the direction of the local RF field (red arrows). (c) Cross-sectional view and simulated distribution of the dominant electrical component ε_x of the optical quasit-TE mode field for a single phase modulator (slot width 160 nm, rail width 210 nm, waveguide height 220 nm). The optical mode is strongly confined to the slot due to electric-field discontinuities at the slot sidewalls. (d) Simulated ε_x-component of the RF mode field of the slot waveguide. The modulation voltage drops across the narrow slot resulting in a high modulation field that has a strong overlap with the optical mode. (e) Transmission versus dc voltage of a MZM having 1 mm long phase shifters. At bias voltages above 3 V, the π-voltage of the device amounts to $U_\pi = 0.5$ V, corresponding to a voltage-length product of $U_\pi L = 0.5$ Vmm. For smaller dc voltages, free charges in the cladding lead to a partial screening of the applied electric field and hence to slightly increased π-voltages for dc operation. (f) High-speed operation: Phase modulation index η vs. frequency for an on-chip RF power of 10 dBm. When using an electric gate field E_gate to increase the conductivity of the slabs, a 3 dB bandwidth of at least 100 GHz can be achieved [20]. The horizontal dotted black lines represent the maximum value (upper line) and a fraction of 70.7% thereof (-3 dB, lower line). (Figure adapted from [15]).

products as small as $U_\pi L = 0.5$ Vmm [20]–[22]. SOH modulators can be designed for low energy consumptions of only a few femtojoule per bit [19], [20] or for high modulation frequencies of up to 100 GHz [21]. Moreover, SOH devices are perfectly suited for advanced modulation formats such as quadrature phase-shift keying (QPSK) and 16-state quadrature-amplitude modulation (16QAM) [22], [23]. The high modulation efficiency of SOH modulators allows to drive the devices directly from binary CMOS output ports of standard field-programmable gate arrays (FPGA) for generating advanced modulation formats without the use of digital-to-analog converters (DAC) or radio-frequency (RF) drive amplifiers [24]. POH modulators stand out due to their high modulation speed and ultra-compact footprint, featuring voltage-length products down to $U_\pi L = 0.05$ Vmm and typical lengths of a few tens of micrometers [25]–[28]. The viability of the devices has been demonstrated in a series of data transmission experiments using binary phase shift keying (BPSK), on-off-keying (OOK) and four-state amplitude shift keying (4-ASK) as modulation formats [25], [26]–[28].

The paper is structured as follows: In Section II, we introduce the principles and the unique features of SOH devices and cover a series of experimental demonstrations. Section III introduces the POH approach and summarizes the corresponding experimental demonstrations, and Section IV gives a comparison of the various modulator concepts. The paper is concluded by an outlook covering current activities and future research directions, see Section V. The Appendix gives details on mathematical models used to estimate modulator performance end efficiency.

II. SOH INTEGRATION

A. The SOH Device Concept

The basic structure of an SOH Mach–Zehnder modulator (MZM) is illustrated in Fig. 1(a) [14], [15]. The MZM comprises two SOH phase modulators that are driven in push-pull mode by a single coplanar transmission line in ground-signal-ground (GSG) configuration. Each of the phase modulators consists of a slot waveguide, which is covered by an organic EO material, see cross-section in Fig. 1(b). The fundamental optical quasi-TE mode is strongly confined to the slot region due to field discontinuities at the slot sidewalls [29], Fig. 1(c). At the same time, the metal strips of the transmission line are electrically connected to the rails of the phase modulators by thin n-doped silicon slabs such that a voltage applied to the transmission line drops across the narrow slot. This results in a strong modulating RF field that overlaps perfectly with the optical quasi-TE mode, see Fig. 1(d). For connecting the slot-waveguide phase shifters to conventional SOI strip waveguides in an MZM configuration, logarithmically tapered strip-to-slot converters are used that have insertion losses of less than 0.1 dB at lengths of less than 10 μm [30].

The basic SOI waveguide structures can be fabricated by widely available CMOS processes, and the EO organic material is then deposited by spin coating. Directly after deposition, the organic material does not show any macroscopic EO effect due to random orientation of the chromophore molecules. To induce macroscopic EO activity, the material is poled by heating it to the glass-transition temperature T_g while applying a dc poling voltage U_{poling} between the floating ground electrodes of the MZM. The resulting poling fields in the slots align the dipolar chromophores as indicated by the dark blue arrows in Fig. 1(b) [20]. While keeping the poling voltage constant, the chip is cooled back to room temperature such that the acentric order of the chromophores is conserved. The RF modulation field of the GSG transmission line, indicated by red arrows in Fig. 1(b), is parallel to the chromophore orientation in the left phase shifter and antiparallel in the phase shifter on the right-hand side, thereby resulting in efficient push-pull operation of the device.

The π-voltages of the SOH MZM are obtained from measuring the transmission as a function of an applied DC voltage, see Fig. 1(e). For a device with 1 mm-long phase shifters, we find a π-voltage U_π of only 0.5 V for bias voltages of more than 3 V, corresponding to a voltage-length product of only $U_\pi L =$ 0.5 Vmm, see Fig. 1(e) [20]. For smaller bias voltages, we observe slightly increased spacings of the transmission dips and hence slightly increased π-voltages, which is attributed to free ions in the cladding that lead to a partial screening of the applied fields at small bias voltages. This effect is only observable for low frequencies and does not impede RF operation.

The modulation speed of the modulators is limited by the *RC* time constant of the slot waveguide structure: The slot corresponds to a capacitor *C,* which is charged and discharged via the resistive silicon slabs, see Fig. 1(d). The EO bandwidth can be increased by applying a static gate voltage between the substrate and the top silicon layer, which increases the conductivity of the slabs by inducing a charge accumulation layer [31]. Applying this technique to a short device of only 500 μm length results in 3 dB bandwidths of more than 100 GHz,Fig. 1(f) [21].

The SOH approach is a general concept, which is not limited to EO modulators only. We have shown that particularly compact and power-efficient phase shifters can be realized by using liquids crystals as a cladding of the SOH waveguide [32], [33]. For a device length of 1.7 mm, we achieved an overall phase shift of approximately 80 π at a voltage of 4 V [32]. Similarly, we could demonstrate pulsed lasing in optically pumped SOH waveguides that have dye-doped polymers as a cladding [34].

B. *Efficiency of SOH Devices*

Energy efficiency is one of the most important metrics of photonic-electronic interfaces. The energy consumption of an EO modulator depends not only on the physical properties of the phase shifters, but also on the electronic design of the feed circuitry. Conventionally, modulators are designed as travelling-wave devices, having a 50 Ω input impedance, matched to the $Z_L = 50\ \Omega$ wave impedance of standard transmission lines and RF cables. For estimating the energy consumption, the device can be modeled by an equivalent circuit consisting of a single load resistor of $R_L = 50\ \Omega$, see Fig. 2(a). The driving source is characterized by an open-circuit voltage of U_0 and an internal impedance of $R_i = 50\ \Omega$ for minimum back reflection and maximum power transfer to the transmission line. The modulator drive voltage is then only half of the open-circuit source voltage, $U_{\mathrm{drive}} = U_0/2$. For simple on-off-keying, the per-bit energy consumption in the modulator can be estimated by considering the power dissipation in the load resistor during one bit slot of duration T_{bit},

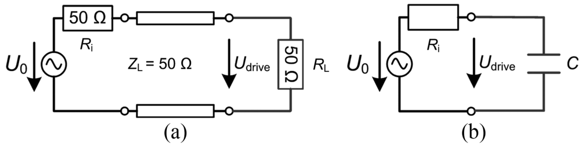

Fig. 2. Equivalent-circuit models of EO modulators. (a) Impedance-matched travelling-wave device featuring an ohmic input load impedance of $RL = 50\,\Omega$, connected to a transmission line having a wave impedance $ZL = 50\ \Omega$ and a signal source with an internal impedance of $Ri.= 50\ \Omega$. The modulator drive voltage is only half the internal source voltage, $U_{\mathrm{drive}} = U_0/2$. For estimating the energy consumption, the device is modeled by a single 50 Ω resistor. (b) Unterminated lumped-element EO modulator represented by a capacitive load *C*. If the device is driven below its R_iC cut-off frequency, the drive voltage reaches a steady-state value which is equal to the open-circuit source voltage, $U_{\mathrm{drive}} = U0$. The energy consumption is then dictated by the power dissipation in the resistor R_i during charging and dis-charging the capacitor. This power dissipation is independent of the exact value of R_i.

$$W_{\mathrm{bit}} = \frac{U_{\mathrm{drive}}^2 T_{\mathrm{bit}}}{4R_L}. \tag{1}$$

This concept leads to comparatively high energy consumptions: For operating voltages of only $U_{\mathrm{drive}} = 1$ V, a load resistance of $R_L = 50\,\Omega$, and a data rate of 10 Gb/s, i.e., a bit duration of $T_{\mathrm{bit}} = 100$ ps, the per-bit energy consumption amounts to 500 fJ/bit.

This energy consumption can be considerably reduced by using SOH devices. First, due to highly efficient EO materials and the thereby decreased voltage-length products of $U_\pi L \approx 0.5$ Vmm, SOH phase shifters can be made much shorter than their all-silicon counterparts that rely on FCD. As a consequence, the length of SOH devices can be kept short in comparison to the RF wavelength of the modulating signal on the chip, and the devices do not need to be designed in an impedance-matched travelling-wave configuration. Instead, the modulators can be operated as purely capacitive loads, as illustrated in Fig. 2(b), assuming that the electronic driver circuitry can be co-integrated in close proximity such that the feed lines can be kept short and impedance matching is not required. Assuming that the device is driven below its R_iC cut-off frequency $f_c = 1/(2\pi R_i C)$, the drive voltage reaches a steady-state value which is equal to the internal source voltage, $U_{\mathrm{drive}} = U_0$. The energy consumption is then dictated by the power dissipation in the resistor R_i during charging and discharging the capacitor. This power dissipation is independent of the exact value of R_i. For non-return-to-zero (NRZ) OOK, the power dissipation can be estimated to be [35]

$$W_{\mathrm{bit}} = \frac{CU_{\mathrm{drive}}^2}{4} = \frac{Q_{\mathrm{bit}} U_{\mathrm{drive}}}{2} \tag{2}$$

where $Q_{\mathrm{bit}} = C\, U_{\mathrm{drive}}/2$ denotes the average charge that has to be transported into the device per bit. Typical capacitances of SOH modulators amount to 200 fF for a 500 μm long device [19]. Assuming a drive voltage of 1 V, this leads to a typical per-bit energy consumption of 50 fJ/bit, which is approximately an order of magnitude smaller than the value estimated for travelling-wave devices.

Besides the operating voltage U_{drive}, Eq. (2) introduces the charge transport Q_{bit} per bit as another important figure of merit (FOM) that characterizes the efficiency of a capacitive EO phase shifter such as a reverse-biased pn-junction, an MOS capacitor, or an SOH or POH slot waveguide structure. To a first-order approximation, the phase shift in such a device is proportional to the charge transport, but independent of the device length: Increasing the length of the phase shifter will not only increase the phase shift for a given variation of refractive index and charge density, but also the active volume and hence the capacitance of the device will be increased, such that the ratio of phase shift $\Delta\varphi$ and the associated charge transfer ΔQ is constant, see Appendix for a more detailed analysis. Let us first consider a continuous-wave (CW) optical signal of vacuum wavelength λ that is phase-modulated by FCD in a silicon strip waveguide of width w and height h. Following the analysis described in the Appendix, the ratio of charge transfer and phase shift for FCD devices can be estimated to be

$$\frac{\Delta Q_{\mathrm{FCD}}}{\Delta \Phi_{\mathrm{FCD}}} = \frac{\lambda \mathrm{whe}}{2\pi B \Gamma_{\mathrm{core}}} \tag{3}$$

where $e = 1.602 \times 10^{-19}$ C is the elementary electric charge, Γ_{core} denotes the field interaction factor of the guided mode with the silicon waveguide core, and $B = 2.7 \times 10^{-21}$ cm^3 is a material constant of silicon that relates the change of the density of holes to the change of the refractive index, see Appendix. Note that the ratio of charge transfer and phase shift given in Eq. (3) is rather insensitive to the exact implementation of the device, since the parameter ranges for waveguide width w and height h are usually determined by the necessity to maintain low-loss single-mode operation of the device. For typical values of $\lambda = 1.55$ μm, $h = 220$ nm, $w = 450$ nm, and $\Gamma_{\mathrm{core}} = 0.8$, we obtain charge transfers of the order of $\Delta Q_{\mathrm{FCD}}/\Delta\phi_{\mathrm{FCD}} \approx 6$ pC/π for devices that are based on FCD.

Similarly, we can estimate the normalized charge transfer for an SOH device, clad by an organic EO material of optical refractive index n_{EO}, EO coefficient r_{33}, and an RF dielectric constant ε_r, see Appendix for more details. In this case, the ratio of charge transfer and phase shift amounts to

$$\frac{\Delta Q_{\mathrm{SOH}}}{\Delta \Phi_{\mathrm{SOH}}} = \frac{\lambda \varepsilon_0 \varepsilon_r h}{2\pi r_{33} n_{\mathrm{EO}}^3 \Gamma_{\mathrm{slot,x}}} \tag{4}$$

where $\varepsilon_0 = 8854 \times 10^{-12}$ As/Vm denotes the vacuum permittivity, and $\Gamma_{\mathrm{slot},x}$ is the field interaction factor of the E_{x}-component of the guided mode field with the EO material in the slot, see Eq. (20) of the Appendix for the mathematical relationship and Fig. 8(a) for numerically calculated values. Also here, the ratio of charge transfer and phase shift is rather insensitive with respect to the device geometry, given the fact that there is only limited flexibility of choosing the height h of a single-mode SOI waveguide. For typical values of $\lambda = 1.55$ μm, $n_{\mathrm{EO}} = 1.7$, $r_{33} = 150$ pm/V, $h = 220$ nm, $\varepsilon_r = 6$, and $\Gamma_{\mathrm{slot},x} = 0.25$, we obtain charge transfers of the order of $\Delta Q_{\mathrm{SOH}}/\Delta\phi_{\mathrm{SOH}} \approx 50$ fC/π. This means that for a given phase shift the charge transport required in an SOH device is more than two orders of magnitude smaller than that for a conventional silicon photonic device relying on FCD. This figure is independent of the length and hence independent of the operation voltage of the device. This confirms the superior efficiency of the SOH approach. Note that the ratio $\Delta Q_{\mathrm{SOH}}/\Delta\phi_{\mathrm{SOH}}$ derived for SOH devices also applies to POH modulators, see Appendix. A more detailed comparison of different FOM for SOH, POH, and FCD modulators is given in Section IV.

C. Advanced EO Materials

Besides the design of the optical waveguide and of the RF feed line, the EO properties of the cladding are of crucial importance for the performance of SOH modulators. Conventionally, the most commonly used cladding materials for SOH integration are polymers doped with EO chromophores [36], [37]. While these guest-host materials exhibit EO coefficients r_{33} as high as 198 pm/V at a wavelength of 1550 nm in bulk material or stacked thin-film layers [38], [39], values measured in SOH devices were much smaller, ranging from 20 to 60 pm/V [36], [37]–[40]. We demonstrated that significantly larger in-device EO coefficients of up to 230 pm/V can be achieved by using monolithic or binary chromophores that do not require a polymer matrix to mitigate dipolar interaction and detrimental head-to-tail orientation of the chromophore molecules [19]. Fig. 3(a), (b), and (c) show different molecular structures of EO materials. YLD124 is an EO chromophore that is usually used in conventional guest-host systems [41], [42], whereas the chromophores DLD164 and PSLD41 are structurally engineered molecules optimized for enhanced poling efficiency when used in monolithic form. For DLD164, Fig. 3(b), pendant coumarin-containing site-isolation groups (depicted in blue) mitigate dipole-dipole interaction and reduce the rotational degrees of freedom of the chromophores from three to two. This improves the chromophore alignment for a given poling field by roughly a factor of two [39]. For PSLD41, Fig. 3(c), perfluoraryl-containing side-groups ("site-isolation groups," depicted in blue) are used to effectively reduce the dipole-dipole interaction of neighboring molecules. The chromophore features a dendrimer structure, consisting of a central connecting motif that links three EO substructures. This results in a spherical shape of the molecule and improved poling efficiency [43].

To investigate the performance of these materials in SOH devices, we apply them to nominally identical modulator chips and measure the π-voltage at dc such that the EO coefficient r_{33} can be derived. Fig. 3(d) depicts the resulting r_{33} as a function of the applied poling field for various materials. This allows calculating the poling efficiency, i.e., the ratio $r_{33}/E_{\mathrm{poling}}$ in the limit of small poling fields, indicated by the straight fitted lines in Fig. 3(d). For a guest-host system of YLD124 (25 wt.%)

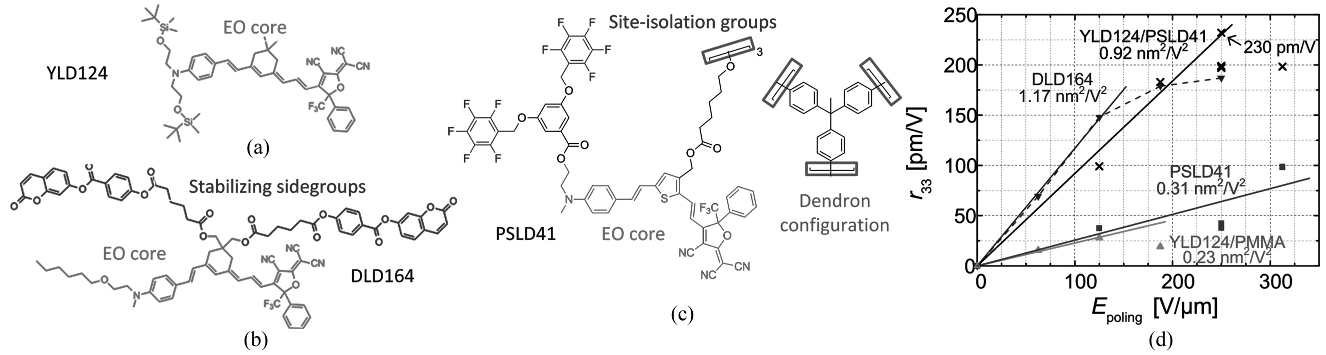

Fig. 3. (a)–(c) Chemical structures of EO chromophores. The EO active cores are drawn in red. The materials DLD164 and PSLD41 consist of structurally engineered chromophores that enable high chromophore densities and a high degree of chromophore orientation during poling. Sidegroups that lead to matrix stabilization and enhancement of molecular orientation are marked in blue. (a) YLD124, used in guest-host systems (PMMA doped with 25 wt% YLD124) or in a binary-chromophore organic glass together with PSLD41 (25:75 wt%). (b) DLD164, used in pure form as a monolithic chromophore. (c) PSLD41, a dendritic molecule that combines three EO substructures, marked in light blue. (d) Measured poling efficiencies r_{33} / E_{poling} for the different organic cladding materials. We find extraordinarily high in-device EO coefficients for DLD164 (190 pm/V) and for the YLD124/PSLD41 mixture (230 pm/V). (Figure adapted from [16]).

in PMMA, we measure small r_{33}-values of less than 29 pm/V only along with low poling efficiencies of 0.23 nm^2/V^2. These values are far below those achieved in the corresponding bulk material [38] and similar to previously reported results in other guest-host systems [36]–[44]. For the pure monolithic chromophore DLD164, we find a much higher poling efficiency of 1.17 nm^2/V^2 and a large r_{33} of up to 190 pm/V, see green trace in Fig. 3(d). For pure PSLD41, both the in-device r_{33} and the poling efficiency are slightly smaller and amount to 97 pm/V and 0.31 nm^2/V^2, respectively, whereas a mixture of YLD124 and PSLD41 (25:75 wt.%) results in an EO coefficient of 230 pm/V which is even higher than that of its constituents with a poling efficiency of 0.92 nm^2/V^2. These findings are in good agreement with results obtained in the corresponding bulk material, where the binary chromophore system YLD124/PSLD41 was found to have an r_{33} coefficient that exceeds even the sum of the r_{33} coefficients of its constituents [45]. The observed r_{33} coefficient of 230 pm/V is the highest reported value in an SOH device until now, and is even higher than previously reported record values of a fully organic MZM, where 137 pm/V was measured [46].

Comparing in-device EO coefficients r_{33} to the values obtained for the corresponding EO bulk materials, we find that poling efficiencies r_{33}/E_{poling} for bulk material are generally higher than for thin layers in SOH devices. However, the thin layers of EO material in SOH devices turn out to be more resilient with respect to dielectric breakdown, such that higher electric poling fields E_{poling} can be applied than in bulk configurations. We attribute the increased resilience to thin-film effects and to a low number of defects in the SOH slot region. The ability to use higher poling fields may even overcompensate the effect of a reduced poling efficiency: For PSLD41, the highest reported bulk EO coefficient amounts to $r_{33} = 90$ pm/V and is achieved for a poling field of 90 V/μm, whereas an r_{33}-coefficient of 98 pm/V was observed in an SOH device for a poling field of more than 300 V/μm, which is far beyond the maximum applicable poling field of 100 V/μm in bulk material. A more detailed discussion can be found in [19].

D. Advanced EO SOH Devices: Modulation at fj/bit and Advanced Modulation Formats

The viability of SOH devices has been demonstrated in a series of experiments. By combining highly efficient EO materials with ultra-short devices that can be operated as purely capacitive loads, MZM with record-low power consumptions were demonstrated [19], [20]. In an OOK signaling experiment, a peak-to-peak drive voltage of only 80 mV$_{\text{pp}}$ was sufficient to keep the measured bit-error ratio (BER) below the hard-decision forward-error correction (FEC) threshold of 4.510^{-3} [47]. This corresponds to a record-low energy consumption of only 0.7 fJ/bit [20]. For a BER below 10^{-9}, a drive voltage of $U_{\text{drive}} = 460$ mV$_{\text{pp}}$ was required, corresponding to a power consumption of 27 fJ/bit. An eye diagram for a peak-to-peak drive voltage of 300 mV$_{\text{pp}}$ is depicted in Fig. 4(a), corresponding to an energy consumption of 10 fJ/bit. These figures are an order of magnitude below the energy consumption of all-silicon MZM relying on FCD [48]. Besides conventional OOK, SOH MZM also support advanced modulation formats such as binary phase shift keying (BPSK) and bipolar amplitude shift keying (ASK), Fig. 4(b) [17]. Using bipolar 4ASK at a symbol rate of 64 GBd, we demonstrated line rates of up to 128 Gb/s [49]. Moreover, QPSK and 16-state quadrature amplitude modulation (16QAM) have been demonstrated with symbol rates (raw data rates) of up to 45 GBd (90 Gb/s) and 40 GBd (160 Gb/s), respectively, see Fig. 4(c) and (d) [22]–[24]. For 16QAM transmission at 28 GBd, the IQ modulator was operated with peak-to-peak drive voltages of 600 mV$_{\text{pp}}$, leading to a power consumption of only 19 fJ/bit [22]. This is the lowest drive voltage and the lowest energy consumption that has so far been reported for a silicon 16QAM modulator at comparable speed.

The high modulation efficiency of SOH devices can be used to greatly simplify the electronic driver circuitry. In particular, it is possible to directly use the binary outputs of state-of-the-art CMOS circuitry for generating the sub-1 V drive signals required to operate the modulator. We have demonstrated generation of simple OOK signals by connecting an SOH MZM

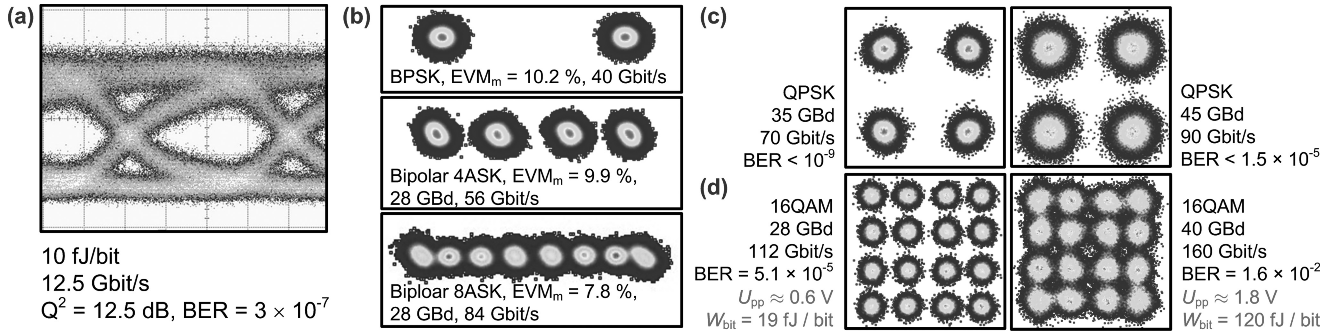

Fig. 4. Experimental demonstration of high-performance SOH modulators. (a) Modulation at ultra-low energy consumption: When operating a short device with high EO efficiency as a capacitive load, good signal quality can be obtained for modulation energies of a few femtojoule per bit [19], [20]. (b) Constellation diagrams for BPSK and bipolar ASK along with the corresponding error-vector magnitudes (EVM). BPSK transmission was found to be error-free. For the bipolar 4ASK (56 Gb/s) and the bipolar 8ASK (84 Gb/s), the measured BER amounted to 2×10^{-6} and 9.7×10^{-3}, respectively [17]. (c) Constellation diagrams of QPSK signals for symbol rates of 35 and 45 GBd [22], [23]. No bit errors were detected within our record length of 62.5 μs for 35 GBd, and the error vector magnitude ($\mathrm{EVM_m}$) indicate error-free signals with BER $< 10^{-9}$. At 45 GBd, the BER amounts to 1.5×10^{-5} and is well below the threshold for hard-decision FEC with 7% overhead. (d) Constellation diagrams of 16QAM-signals for symbol rates of 28 and 40 GBd. For 28 GBd, the IQ modulator was operated with peak-to-peak voltages of $U_{\mathrm{pp}} = 0.6$ V, leading to a power consumption of 19 fJ/bit and a BER of 5.1×10^{-5}—well below the threshold for second-generation hard-decision FEC. For 40 GBd, the BER is still below the 2.4×10^{-2} threshold for soft-decision FEC with 20 % overhead. (Figure adapted from [15]).

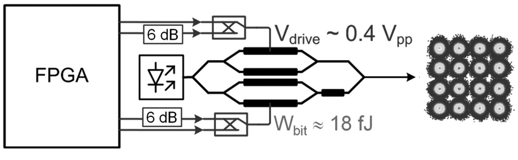

Fig. 5. DAC-less amplifier-less generation of 16QAM signals by driving a highly efficient SOH IQ modulator from the binary CMOS outputs of a FPGA via a purely passive combiner network. The four-level drive signals for the in-phase (I) and quadrature (Q) arm of the modulator are generated by superimposing two binary signals, one of which is attenuated by a factor 2 in amplitude (6 dB). The resulting four-level signal has a peak-to-peak amplitude of 400 m V_{pp}. and is sufficient to generate high-quality 16QAM signals at a symbol rate of 10 GBd and an energy consumption of only 18 fJ/bit [24].

directly to a standard 10 Gb/s GTX transmitter port of a Xilinx Virtex-7 FPGA without using an intermediate drive amplifier [50]. More recently, we have extended this concept to advanced modulation formats by demonstrating that 16QAM signals at 13 GBd can be generated without using DAC or drive amplifiers [24]. The underlying concept is illustrated in Fig. 5. A highly efficient SOH IQ modulator is connected to four binary CMOS outputs of a FPGA via a purely passive combiner network. The four-level drive signals for the in-phase (I) and quadrature (Q) MZM are generated by a purely passive combiner network which superimposes two binary signals, one of which is attenuated by a factor 2 in amplitude (6 dB). The resulting four-level signal has a peak-to-peak amplitude of $400\ \mathrm{mV_{pp}}$, which is sufficient to generate 16QAM signals that maintain a BER below the threshold of hard-decision FEC with 7% overhead, even after propagation over 100 km [24]. The associated energy consumption amounts to only 18 fJ/bit and is smaller by more than an order of magnitude than that of conventional 16 QAM transmitters.

III. POH INTEGRATION

A. The POH Device Concept

The basic idea of the SOH concept can be transferred to plasmonic waveguides, leading to POH devices. In POH phase shifters, both the optical and the RF signal are guided by thin metal sheets, see Fig. 6(a) and (b) [25]. The two sheets form a metal slot waveguide in which light propagates as a SPP mode. The slot is filled with an EO polymer, and phase modulation is achieved by applying a voltage to the metal sheets. The tight confinement of the SPP modes leads to an overlap of optical and RF field that is even better than for POH waveguides. As a consequence, record-low voltage-length products down to $U_\pi L = 0.05$ Vmm were demonstrated in POH devices [27]. Moreover, POH modulators offer speed advantages compared to their SOH counterparts: In SOH devices, charging and discharging of the slot capacitance through the resistive silicon slabs leads to an intrinsic *RC* time constant which may limit the speed of the device as described in Section II-A [21]. POH devices are not affected by such intrinsic limitations, since the slot capacitance is connected to the source by a highly conductive metal film, within which free carriers rearrange virtually instantaneously under the influence of an externally applied voltage. Moreover, extrinsic speed limitations caused by a nonzero internal impedances of real-world voltage sources can be safely neglected in POH devices due to the extraordinarily small capacitance, which can be of the order of $C = 3$ fF [27]. Together with an internal source impedance of typically $R_i = 50\ \Omega$, this leads to an *RC*-related bandwidth of the order of 1 THz, which is far above the limitations imposed by current electronic drive circuitry. This in combination with the essentially instantaneous response of the organic EO cladding material frees POH devices from any appreciable limitations of the modulation speed.

Since plasmonic waveguides still exhibit substantial propagation loss, it is advantageous to embed the POH into a network of conventional dielectric SOI waveguides that allow low-loss transport of light across the photonic chip, see Fig. 6(c). For efficient mode conversion between the photonic strip waveguide and the plasmonic slot waveguide, transitions between the dielectric transport waveguides and the POH phase shifter sections are realized by inversely tapered SOI structures that connect to the input of a tapered SPP slot waveguide, Fig. 6(d) [25]. The coupling structures are approximately 3 μm long and feature power conversion efficiencies of more than 80% [25].

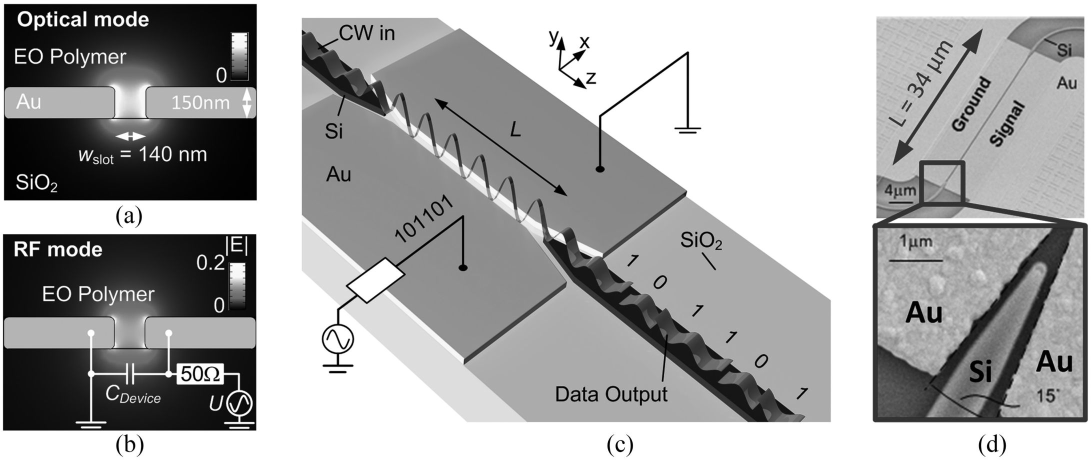

Fig. 6. POH phase modulator. (a) Optical mode: Light is guided as a SPP mode of a metal slot waveguide. The slot is filled with an EO polymer, and phase modulation is achieved by applying a modulating voltage to the metal sheets. (b) RF mode: The applied voltage drops entirely across the slot, leading to perfect overlap of the RF mode with the optical mode in the EO cladding. (c) POH modula-tor connected to dielectric SOI waveguides: Current plasmonic waveguides feature high propagation losses. It is therefore advantageous to embed the POH phase modulator into conventional silicon photonic circuitry that uses low-loss dielectric waveguides to transport light across the chip. (d) Mode converter between a photonic strip waveguide and a plasmonic slot waveguide made from gold (Au). The converter structures are approximately 3 μm long and feature power conversion efficiencies of more than 80 %. (Figure modified from [25]).

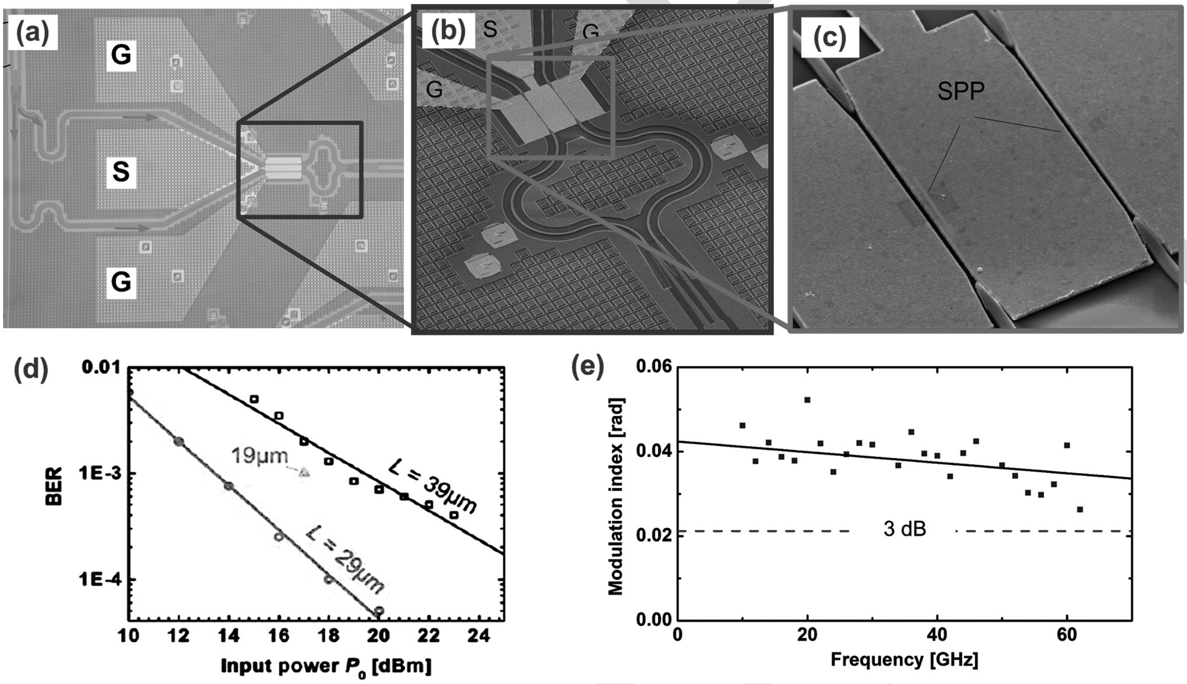

Fig. 7. Experimental demonstration of a POH MZM. (a) The POH phase shifters are embedded into a Mach–Zehnder interferometer realized by conventional SOI strip waveguides. Electrical signals are fed to the device using a GSG electrode configuration. (b), (c) Zoom-in of the POH phase shifters and the transitions between dielectric SOI waveguides and plasmonic slot waveguides. (d) BER versus optical input power $P0$ into the POH MZM for different phase shifter lengths L. A phase shifter length of $L = 29$ μm leads to a compromise between the optical insertion loss and the modulation depth of the signal. (e) Frequency response of a 29 μm-long POH phase modulator. The graph depicts the modulation index as a function of the modulating frequency for a sinusoidal RF modulation signal delivered by a 50 Ω generator with an available power of –10 dBm. Grey dots indicate measured values, and the black line represents a linear fit to this data. The frequency response is essentially flat over the measurement range, except for a small frequency-dependent decay and some oscillations that we attribute to reflections from the POH modulator that acts as a capacitive load. To indicate the 3 dB limit, we include a dashed line at half the modulation index in the low-frequency limit. The device features a 3 dB bandwidth of significantly more than 60 GHz.

B. Experimental Demonstrations of POH Devices

The viability of POH EO modulators was demonstrated in first data transmission experiments using BPSK and conventional on-off keying (OOK) at data rates of 40 Gb/s as well as bipolar ASK with four levels (4ASK) at 90 Gb/s [25]–[28]. The MZM device layout and the experimental results for 40 Gb/s OOK are depicted in Fig. 7 [26]. The device consists of a Mach–Zehnder interferometer realized by conventional SOI strip waveguides with embedded POH phase shifter sections, see Fig. 7(a), (b), and (c).

Electrical signals are fed to the device by GSG electrodes, and appropriate poling of the POH phase shifters is used to enable

TABLE I
COMPARISON OF FOM OF DIFFERENT MODULATOR TYPES

Modulator Type	$U_\pi L$ [Vmm]	a [dB/mm]	$aU_\pi L$ [dBV]	ΔQ/$\Delta\varphi$[fC/π]	$W_{\pi,1\,\mathrm{dB}}$, [fJ]
pn-depletion	10.00	1	10	> 1000	5000
SOH	0.5	2	1	50	25
POH	0.05	200	10	12	60

efficient push-pull operation as described for SOH devices in Section II-A. The performance of the generated data signal depends predominantly on the length L of the phase shifters: Giving the limited RF drive power, short devices lead to an insufficient modulation depth, whereas long devices suffer from excessive optical insertion loss and hence degrade the signal quality as well.Fig. 7(d) shows measured BER versus optical input power P_0 that is launched into MZM of different phase shifter lengths L. A length of $L = 29\ \mu$m leads to the lowest BER for a given launch power and hence represents a good compromise between the optical insertion loss and the modulation depth of the signal. To characterize the high-speed behavior of the device, we measured the EO response of a 29 μm long POH phase modulator, see Fig. 7(e) which depicts the modulation index as a function of the modulation frequency for a 29 μm-long POH phase modulator. The device was driven by sinusoidal signal generator having an impedance of 50 Ω and an available RF power of –10 dBm. Grey dots indicated measured values, and the black line represents a linear fit to the measured data. The frequency response features a small frequency-dependent decay and some oscillations that we attribute to back-reflections due to the capacitive input impedance of the POH modulator. The 3 dB bandwidth of the device is significantly larger than the measurement range of 60 GHz. The decay of the frequency response is attributed to RC time constants that result from an interaction of the device capacitance with the 50 Ω internal impedance of the source and additional parasitic impedances of the feed circuitry.

IV. COMPARISON OF DEVICE CONCEPTS AND PERFORMANCE

When evaluating the performance of POH modulators in comparison to SOH devices and conventional depletion-type FCD modulators, several FOM need to be considered, see Table I. Note that for all FOM described in this section, smaller values correspond to superior device performance. This somewhat counter-intuitive definition of the FOM is chosen to adhere to conventional modulator performance metrics that are commonly used in the literature. Modulator efficiency is normally expressed by the product of π-voltage U_π and device length L. In this respect, current SOH devices show more than an order of magnitude of improvement [20] compared to conventional depletion-type FCD modulators [2]–[9]. POH devices improve this FOM by another order of magnitude [27] due to an enhanced interaction of the guided light and the RF modulation field within the EO material. For a more detailed quantitative analysis of the enhanced interaction, we consider the phase shift $\Delta\varphi$ accumulated along a phase-shifter waveguide of length L under the influence of an externally applied voltage,

$$\Delta\Phi = -k_0 \Delta n_{\mathrm{e}} L. \qquad (5)$$

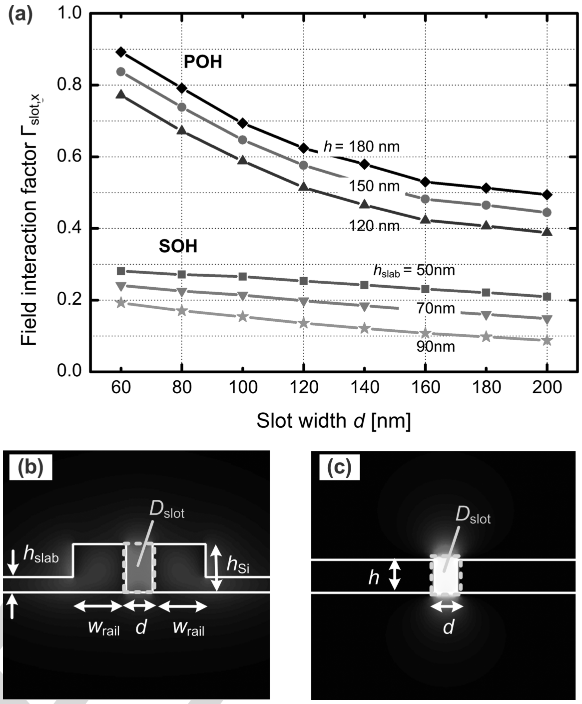

Fig. 8. Field interaction of the optical mode with the EO cladding material. (a) Field interaction factor γ_{slot} of the optical mode with the EO cladding material in the slot region D_{slot} as a function of slot width d for both POH and SOH waveguides at a wavelength of 1550 nm. The field interaction factor $\gamma_{\mathrm{slot,x}}$ as defined in Eq. (20) of the Appendix takes into account both the effects of spatial field overlap and of reduced group velocity. For the SOH device, the height of the silicon waveguides amounts to $hSi = 220$ nm, and a value of $w_{\mathrm{rail}} = 240$ nm was chosen for the width of the silicon rails, which represents approximately the optimum for a maximum field interaction factor $\gamma_{\mathrm{slot,x}}$. In general, POH devices feature a 2.5–3.5 times larger field interaction factor than SOH devices due to the tight confinement of the plasmonic mode to the slot region and due to a reduced group velocity of the plasmonic slot mode. For POH devices, $\gamma_{\mathrm{slot,x}}$ decreases as the height h of the metal is reduced, since the mode field reaches further out of the slot region D_{slot}. Similarly, for SOH devices, γ_{slot} decreases as the height h_{slab} of the silicon slabs is increased, since the optical mode field reaches out further into the slab region and the intensity within D_{slot} reduces. For the width of the silicon rails, the optimum value of $w_{\mathrm{rail}} \approx 240$ nm represents a trade-off between strong field confinement in the silicon core for very wide rails and deep penetration of the mode field into the cladding for very narrow rails. (b) Cross section and mode field of an SOH phase shifter ($h_{\mathrm{Si}} = 220$ nm, $w_{\mathrm{rail}} = 240$ nm, $d = 120$ nm, $h_{\mathrm{slab}} = 70$ nm); (c) Cross section and mode field of a POH phase shifter ($h = 150$ nm, $d = 100$ nm). The quasi-TE mode of the POH structure features a significantly stronger confinement to the slot region than its SOH counterpart.

In this relation, $k_0 = 2\pi c/l$ is the optical vacuum wavenumber at a vacuum wavelength λ, and Δn_e denotes the change of the effective refractive index $n_e = \beta/k_0$ of the waveguide mode as a consequence of the applied modulation voltage U. For both SOH and POH devices, Δn_e can be approximately expressed by the voltage U, the EO coefficient r_{33} of the cladding material, the slot width d, and the field interaction factor $\Gamma_{\mathrm{slot,x}}$of the E_{x}-component of the optical quasi-TE mode with the EO material in the slot region D_{slot}, see Fig. 8 (b) and (c) and Eqs. (18)–(20) of the Appendix. This leads to the relation

$$\Delta\Phi = \frac{1}{2} n_{\mathrm{EO}}^3 r_{33} \frac{U}{d} \Gamma_{\mathrm{slot,x}} k_0 L \qquad (6)$$

where n_{EO} denotes the refractive index of the EO cladding without any voltage applied to the device, and where $\Gamma_{\mathrm{slot,x}}$is given by Eq. (20) in the Appendix. From these relations, we can derive the voltage-length product required to obtain a phase shift of π,

$$U_\pi L = \frac{2\pi d}{n_{\mathrm{EO}}^3 r_{33} k_0 \Gamma_{\mathrm{slot,x}}}. \tag{7}$$

For a given EO material, POH devices feature a smaller $U_\pi L$ FOM due to the fact that the field interaction factor $\Gamma_{\mathrm{slot,x}}$ of the optical mode with the slot region of POH devices can be 2.5 − 3.5 times larger than for SOH devices, see Fig. 8(a). This is due to both the tight confinement of the plasmonic mode to the slot region, see Fig. 8(b) and (c), and the reduced group velocity of the plasmonic slot waveguide mode. Note that the field interaction factor $\Gamma_{\mathrm{slot,x}}$ as defined in Eq. (20) of the Appendix already accounts for effects of group velocity.

Another important FOMof EO modulators results from the fact that the device length is related to the insertion loss via the propagation loss *a* in the phase shifter section. The quantity *a* is usually expressed in dB/mm. For pn-depletion-type phase shifters, propagation losses are mainly caused by doping, and typically amount to approximately 1 dB/mm. For SOH devices, doping doses can be kept lower in the active region of the waveguide, and the associated propagation losses are expected to stay below 1 dB/mm. In addition, SOH devices experience structure-related propagation losses, which are attributed to sidewall roughness of the slot waveguides. It has been shown that asymmetric slot waveguides and optimized fabrication techniques can reduce structure-related propagation losses to less than 1 dB/mm [51]. For the overall propagation loss of a doped slot waveguide after optimization, we hence estimate an upper boundary of 2 dB/mm—slightly worse than for the pn-depletion-type device. Plasmonic slot waveguides have considerably higher losses of the order of 400 dB/mm for current devices based on Au structures [26], which might be reduced to 200 dB/mm by replacing Au with Ag [28]. In this context, it is important to consider that POH devices are significantly shorter than their SOH or depletion-type counterparts, which strongly mitigates the loss issue. This is expressed by the product of the propagation loss *a* and the $U_\pi L$ FOM—see fourth column in Table I. The resulting π-voltage-loss product has the unit dB V; it corresponds to the product of the phase-shifter insertion loss and the π-voltage and can be interpreted as the π-voltage of a device having a 1 dB insertion loss or, equivalently, as the insertion loss of a device having a π-voltage of 1 V. The SOH devices feature the lowest π-voltage-loss product $aU_\pi L \approx 1$ dB V, whereas the corresponding numbers for both depletion-type devices are one order of magnitude higher. Interestingly, due to their small voltage-length product, POH modulators show similar performance as depletion-type modulators regarding the π-voltage-loss product. The fifth column of Table I specifies the charge ΔQ that has to be transferred to the device to achieve a phase shift of $\Delta\phi = p$. As explained in Section II-B and in the Appendix, this number is rather insensitive to the exact implementation of the device and can therefore be taken as an FOM for the efficiency of the underlying phase modulation mechanism. For SOH devices, a ratio of $\Delta Q/\Delta\phi \approx 50$ fC/π was estimated according to Eq. (4) in Section II-B using typical values of $\lambda = 1.55\,\mu$m, $n_{\mathrm{EO}} = 1.7$, $r_{33} = 150$ pm/V, $h = 220$ nm, $\varepsilon_r = 6$, and $\Gamma_{\mathrm{slot},x} = 0.25$. The same relation can be used for POH devices, but with a reduced thickness $h = 150$ nm of the metal layer and an enhanced field interaction factor of the order of $\Gamma_{\mathrm{slot},x} = 0.70$. This leads to a ratio of $\Delta Q/\Delta\phi \approx 12$ fC/π. All these numbers are to be understood as estimates indicating the order of magnitude—for FCD, our analysis given in Section II-B leads to a value of $\Delta Q/\Delta\phi \approx 6000$ fC/π, where optimization of the optical mode overlap with the doping was not yet considered.

Combining the aforementioned FOM, we can also quantify the power consumption of the various modulator types. For comparability, we consider devices having an insertion loss of 1 dB, hence requiring an operation voltage of $U = aU_\pi L/1$ dB to produce a phase shift of π. At the same time, we can calculate the charge transport associated with a π phase shift to be $Q = \Delta Q/\Delta\phi \times p$. As discussed in Section II-B, the energy consumption associated with this charge transport is dictated by the power dissipation in a series resistor R_i during charging and discharging the capacitance $C = Q/U$ of the modulator. This energy dissipation is independent of the exact value of R_i and, for a single charging process, can be estimated to be $W = QU/2$ [35]. We may hence estimate the energy dissipation W_π, 1 dB associated with a phase shift of π in a device having a 1 dB insertion loss,

$$W_{\pi,1\ \mathrm{dB}} = \frac{1}{2} \times \frac{\Delta Q}{\Delta\Phi}\pi \times \frac{aU_\pi L}{1\ \mathrm{dB}}. \tag{8}$$

This FOMis indicated in the last column of Table I. The best power efficiency is obtained using SOH devices. POH devices require the smallest charge transport to achieve a π phase shift, but they suffer from high propagation losses and hence need to be kept short. This leads to higher operation voltages and hence to a higher energy consumption. Still, POH devices have distinct advantages when it comes to device footprint, enabling modulator lengths of only several tens of micrometers. Moreover, the superior modulation bandwidth of POH devices makes them particularly well suited for applications in THz EO modulation and signal processing. Note that the numbers given here for POH modulators were obtained from first proof-of-concept experiments, whereas pn-depletion-type devices have been optimized over many years.

V. SUMMARY AND OUTLOOK

We have given an overview on recent progress in SOH and POH integration. The concepts combine highly efficient organic EO materials with silicon photonic and plasmonic waveguides. This enables highly efficient modulators with unprecedented performance and compactness. Experimental demonstrations of SOH devices include low-power operation at an energy consumption of a few femtojoule per bit, ultra-fast modulation at frequencies of up to 100 GHz, as well as IQ signaling using advanced modulation formats such as QPSK and 16QAM. POH modulators stand out due to an ultra-compact footprint and due to the absence of practically relevant intrinsic speed limitations.

Current research in the field of SOH EO modulators aims at further increasing the device performance. We have recently demonstrated that SOH devices do not only support 100 Gb/s on-off-keying (OOK) [52], but also 4ASK signaling at symbol rates of 64 GBd—both at room temperature and at 80 C [49]. Beyond these experiments, there is still a series of practical device-related aspects that need systematic investigation in both SOH and POH modulators. As an example, drift of the operating point, which is well known and thoroughly investigated in $\mathrm{LiNbO_3}$ [53] and other devices with insulating EO layer, is also observed in SOH and POH devices and requires further investigation.

Another branch of research concentrates on improved organic EO materials. Currently, in most material systems, less than 15% of the EO activity inherent in the chromophores is translated to macroscopic EO effects by poling, and the poling efficiency depends on the poling configuration. Improved quantum and statistical mechanical (multiscale) theoretical methods [54]–[59] have led to new classes of organic EO materials and to systematic improvements of the poling efficiency, enabling macroscopic EO coefficients r_{33} in excess of 500 pm/V in thin films [54], [55]. Theoretical calculations also suggest that new chromophores with significantly improved molecular first-order hyperpolarizability are possible [54], which may even lead to EO coefficients r_{33} in excess of 1000 pm/V, thereby enabling SOH modulators with π-voltages of less than 100 mV. Moreover, theoretical guidance has also helped to reduce optical loss through control of the homogeneity of the material refractive index.

Besides improving of EO coefficients, systematic investigation and optimization of thermal and photochemical stability of EO cladding materials is subject of ongoing research. Thermal stability is defined by lattice hardness and usually quantified by the glass transition temperature T_g of the material [55]. A glass transition temperature of $T_g = 150$ C is adequate to satisfy Telcordia standards, and such temperatures are easily achieved by crosslinking chemistry, for which values of $T_g = 200$ C are routinely obtained [55]. A specific advantage of organic EO materials is that a variety of parameters such as EO activity, optical loss, dielectric permittivity, lattice hardness, material compatibility, and material processability can be simultaneously optimized by systematic chemical modification and by molecular engineering of the material. We believe that focused material-related research activities in the future will help to unlock the full potential of theory-guided design and synthesis of functional materials for both SOH and POH devices.

APPENDIX
CHARGE TRANSFER IN OPTICAL PHASE SHIFTERS

SOH and POH EO devices show superior efficiency in comparison to conventional silicon photonic modulators based on FCD. To quantify this advantage, we consider first a conventional phase shifter based on an SOI strip waveguide of width w and height h, which exploits refractive index changes in the silicon waveguide core due to modulation of the free-carrier density, see Fig. 9(a) for an illustration of the waveguide cross section. For the analysis, we use a time and space dependence of the form $\exp(j\omega t - j\beta z)$, where $\omega = 2\pi c/l$ denotes the angular frequency of light with a vacuum wavelength λ, while β is the modal propagation constant along the propagation direction z. The phase shift $\Delta\varphi$ accumulated along a waveguide of length L can then be calculated to be

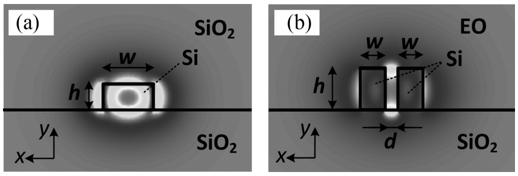

Fig. 9. Schematic cross section of silicon photonic phase shifters. (a) Conventional phase shifter, exploiting refractive index changes due to FCD in the silicon (Si) waveguide core. (b) Slot-waveguide SOH phase shifter, exploiting the refractive index change in the organic EO cladding. In both structures, electric contacts have been omitted for simplicity.

$$\Delta\Phi = -k_0 \Delta n_\mathrm{e} L, \quad k_0 = \frac{2\pi}{\lambda}. \tag{9}$$

In this relation, Δn_e denotes the change of the effective refractive index $n_e = \beta/k_0$ of the waveguide mode as a consequence of free-carrier injection or depletion. In silicon, the carrier-induced refractive index change is dominated by the contribution of holes and can be approximated by

$$\delta n_\mathrm{Si} = -8.36 \times 10^{-18}\mathrm{cm}^{2.4} \times N_h^{0.8} \tag{10}$$

where N_h denotes the density of holes [60]. The exponent of 0.8 makes the relationship of Eq. (10) slightly nonlinear, but we may use a linear approximation which is valid in the vicinity of a typical reference hole densities of $N_\mathrm{h0} = 10^{17}\ \mathrm{cm}^{-3}$,

$$\Delta n_\mathrm{Si} = -B \times \Delta N_h \tag{11}$$

where $\Delta N_h = N_h - N_\mathrm{h0}$ denotes the deviation of the hole density from the reference hole density N_h0, and where $\Delta n_\mathrm{Si} = \delta n_\mathrm{Si}(N_h) - \delta n_\mathrm{Si}(N_\mathrm{h0})$is the corresponding refractive index change. The quantity $B = 2.7 \times 10^{-21}\mathrm{cm}^3$ is a constant that relates the change of the hole density in silicon to the change of the refractive index. Within the SOI waveguide, both the change of the hole density $\Delta N_h(x, y)$ and the refractive index change $\Delta n_\mathrm{Si}(x, y)$depend on the lateral coordinates x and y, and the corresponding change of the effective refractive index must hence be evaluated by an overlap integral in terms of the vectorial modal fields $\underline{\mathcal{E}}_0(x, y)$ and $\underline{\mathcal{H}}_0(x, y)$ of the fundamental waveguide mode [61],

$$\Delta n_\mathrm{e} = \frac{c\varepsilon_0 n_\mathrm{Si} \iint_{-\infty}^{\infty} \Delta n_\mathrm{Si}(x, y) \left|\underline{\mathcal{E}}_0(x, y)\right|^2 \mathrm{d}x\mathrm{d}y}{\iint_{-\infty}^{\infty} \mathrm{Re}\left\{\underline{\mathcal{E}}_0(x, y) \times \underline{\mathcal{H}}_0^*(x, y)\right\} \cdot \mathbf{e}_z \mathrm{d}x\mathrm{d}y}. \tag{12}$$

In this relation, $n_\mathrm{Si} \approx 3.48$ is the refractive index of the silicon core at the reference hole density of $N_\mathrm{h0} = 10^{17}\ \mathrm{cm}^{-3}$. Eq. (12) indicates that the performance of conventional silicon-based phase shifters can be optimized by designing the waveguide such that the hole density changes $\Delta N_h(x, y)$ and the associated refractive variations $\Delta n_\mathrm{Si}(x, y)$ occur in a region where the modal field $\underline{\mathcal{E}}_0(x, y)$ is strong [9].

For a coarse estimation of the device efficiency, we may neglect this effect and simplify Eq. (12) by assuming that holes are injected or depleted homogeneously in the cross section of the waveguide core. As a consequence, both $\Delta N_h\,(x,y)$ and $\Delta n_{\mathrm{Si}}\,(x,y)$ assume constant values of $\Delta N_{h,\mathrm{core}}$ and $\Delta n_{\mathrm{Si,core}}$ within the waveguide core and are zero in the cladding. Note that this is equivalent to assuming that the square of the mode field magnitude $|\underline{\varepsilon}_0\,(x,y)|^2$ can be approximated by a constant corresponding to its average value within the waveguide core. It is then irrelevant how injected or depleted holes are distributed over the cross section of the core; only the total number of transferred holes matters. Eq. (12) can then be approximated by the relation

$$\Delta n_{\mathrm{e}} = \Gamma_{\mathrm{core}} \Delta n_{\mathrm{Si,core}} \tag{13}$$

where Γ_{core} denotes the field interaction factor of the guided mode with the silicon waveguide core,

$$\Gamma_{\mathrm{core}} = \frac{c\varepsilon_0 n_{\mathrm{Si}} \iint_{D_{\mathrm{core}}} |\underline{\varepsilon}_0(x,y)|^2 \mathrm{d}x\mathrm{d}y}{\iint_{-\infty}^{\infty} \mathrm{Re}\left\{\underline{\varepsilon}_0\,(x,y) \times \underline{\mathcal{H}}_0^*\,(x,y)\right\} \cdot \mathbf{e}_z \mathrm{d}x\mathrm{d}y}. \tag{14}$$

In this relation, the integration domain D_{core} of the area integral in the numerator extends over the silicon waveguide core only. Combining Eqs. (9), (11), and (13), the phase shift can be related to the charge ΔQ of the injected holes,

$$\Delta\Phi_{\mathrm{FCD}} = \Gamma_{\mathrm{core}} k_0 \frac{B\,\Delta Q_{\mathrm{FCD}}}{\mathrm{ewh}} \tag{15}$$

where the charge ΔQ_{FCD} is obtained from the elementary charge $e = 1.602 \times 10^{-19}$ C multiplied by the total number of holes within the volume $V = whL$ of the waveguide core,

$$\Delta Q_{\mathrm{FCD}} = e\,w\,h\,L\,\Delta N_h. \tag{16}$$

Solving Eqs. (15) and (16) for the ratio $\Delta Q_{\mathrm{FCD}}/\Delta\phi_{\mathrm{FCD}}$ leads to Eq. (3) of the main text.

Similarly, we can estimate the phase-shift related charge transfer in SOH devices. To this end let us consider a slot waveguide of length L having a cross section as depicted in Fig. 9 (b) with a voltage U applied between the two silicon rails. The phase shift $\Delta\varphi$ accumulated along the waveguide is again calculated according to Eq. (9), where the change Δn_e of the effective refractive index of the mode can be approximated by an overlap integral of the mode field with the local index change $\Delta n_{\mathrm{EO}}\,(x,y)$ of the EO cladding [61],

$$\Delta n_{\mathrm{e}} = \frac{c\varepsilon_0 n_{\mathrm{EO}} \iint_{-\infty}^{\infty} \Delta n_{\mathrm{EO}}\,(x,y)\left|\underline{\varepsilon}_{0,x}\,(x,y)\right|^2 \mathrm{d}x\mathrm{d}y}{\iint_{-\infty}^{\infty} \mathrm{Re}\left\{\underline{\varepsilon}_0\,(x,y) \times \underline{\mathcal{H}}_0^*\,(x,y)\right\} \cdot \mathbf{e}_z \mathrm{d}x\mathrm{d}y}. \tag{17}$$

In this relation, n_{EO} denotes the refractive index of the EO cladding seen by the dominant electric field component ε_x of the optical quasi-TE mode without any voltage applied to the device. Similarly, $\Delta n_{\mathrm{EO}}(x,y)$ denotes the local voltage-induced change of the refractive index that affects the optical ε_x-component. The overlap integral in the numerator of Eq. (17) contains only the *x*-component $\underline{\varepsilon}_{0,x}\,(x,y)$ of the vectorial electric mode field $\underline{\varepsilon}_0\,(x,y)$. For simplicity, we may assume that the modulating RF field features only an *x*-component which assumes a constant value of $E_{\mathrm{mod},x} = U/d$ in the slot region D_{slot} and which is negligible outside. Here, D_{slot} denotes a rectangular region having the width and the height of the slot, see Fig. 8(b) and (c). Using these assumptions, the refractive index change of the cladding can be assumed to have a constant value of $\Delta n_{\mathrm{EO,slot}}$ in the slot and to be zero elsewhere, where

$$\Delta n_{\mathrm{EO,slot}} = -\frac{1}{2} n_{\mathrm{EO}}^3 r_{33} \frac{U}{d}. \tag{18}$$

In this relation, the quantity r_{33} denotes the EO coefficient of the cladding for electric fields oriented in parallel to the material's active optical axis, which is aligned along the *x*-direction of the waveguide coordinate system. The associated change of the effective mode index can now be estimated by multiplying the refractive index change $\Delta n_{\mathrm{EO,slot}}$ in the slot with the field interaction factor $\Gamma_{\mathrm{slot,x}}$ of the mode with the slot region D_{slot},

$$\Delta n_{\mathrm{e}} = \Gamma_{\mathrm{slot,x}} \Delta n_{\mathrm{EO,slot}} \tag{19}$$

where

$$\Gamma_{\mathrm{slot,x}} = \frac{c\varepsilon_0 n_{\mathrm{EO}} \iint_{D\mathrm{slot}} |\underline{\varepsilon}_{0,x}(x,y)|^2 \mathrm{d}x\mathrm{d}y}{\iint_{-\infty}^{\infty} \mathrm{Re}\left\{\underline{\varepsilon}_0\,(x,y) \times \underline{\mathcal{H}}_0^*\,(x,y)\right\} \cdot \mathbf{e}_z \mathrm{d}x\mathrm{d}y}. \tag{20}$$

In this relation, the area integral in the numerator extends only over the slot region D_{slot}. Note that Eq. (20) can also be applied to POH devices, where it accounts also for effects of reduced group velocity of the plasmonic slot waveguide mode.

The charge transfer associated with applying a voltage U to the slot waveguide can be estimated by approximating the slot waveguide by a parallel-plate capacitor filled with the EO polymer of relative permittivity ε_r. The associated capacitance amounts to $C = \varepsilon_0\varepsilon_r hL/d$, leading to a charge transfer of

$$\Delta Q_{\mathrm{SOH}} = \varepsilon_0\varepsilon_r \frac{hL}{d} U. \tag{21}$$

Combining Eqs. (9), (18), (19), and (21), the phase shift can be related to the charge ΔQ of the injected holes,

$$\Delta\Phi_{\mathrm{SOH}} = \Gamma_{\mathrm{slot,x}} k_0 \frac{r_{33} n_{\mathrm{EO}}^3\,\Delta Q_{\mathrm{SOH}}}{\varepsilon_0\varepsilon_r h}. \tag{22}$$

Solving Eq. (22) for the ratio $\Delta Q_{\mathrm{SOH}}/\Delta\phi_{\mathrm{SOH}}$ leads to Eq. (4) of the main text. Note that the derivation of Eq. (22) is independent from the material of the waveguide rails through which the voltage is applied to the EO material. All relations obtained for SOH phase shifters can hence be directly transferred to POH devices.

REFERENCES

[1] J. S. Orcutt, B. Moss, C. Sun, J. Leu, M. Georgas, J. Shainline, E. Zgraggen, H. Li, J. Sun, M. Weaver, S. Urošević, M. Popović, R. J. Ram, and V. Stojanović, "Open foundry platform for high-performance electronic-photonic integration," *Opt. Exp.*, vol. 20, no. 11, pp. 12222–12232, 2012.

[2] G. T. Reed, G. Mashanovich, F. Y. Gardes, and D. J. Thomson, "Silicon optical modulators," *Nature Photon.*, vol. 4, no. 8, pp. 518–526, 2010.

[3] P. Dong, X. Liu, S. Chandrasekhar, L. L. Buhl, R. Aroca, and Y.-K. Chen, "Monolithic silicon photonic integrated circuits for compact 100+ Gb/s coherent optical receivers and transmitters," *IEEE J. Sel. Topics Quantum Electron.*, vol. 20, no. 4, pp. 150–157, Jul./Aug. 2014.

[4] P. Dong, C. Xie, L. Chen, L. L. Buhl, and Y.-K. Chen, "112-Gb/s monolithic PDM-QPSK modulator in silicon," *Opt. Exp.*, vol. 20, no. 26, pp. B624–B629, 2012.

[5] D. J. Thomson, F. Y. Gardes, Y. Hu, G. Mashanovich, M. Fournier, P. Grosse, J.-M. Fedeli, and G. T. Reed, "High contrast 40Gbit/s optical modulation in silicon," *Opt. Exp.*, vol. 19, no. 12, pp. 11507–11516, 2011.

[6] W. M. Green, M. J. Rooks, L. Sekaric, and Y. A. Vlasov, “Ultra-compact, low RF power, 10 Gb/s silicon Mach–Zehnder modulator,” *Opt. Exp.*, vol. 15, no. 25, pp. 17106–17113, 2007.

[7] J. Fujikata, J. Ushida, Y. Ming-Bin, Z. ShiYang, D. Liang, P. Lo Guo-Qiang, D.-L. Kwong, and T. Nakamura, “25 GHz operation of silicon optical modulator with projection MOS structure,” presented at the Optical Fiber Communication Conf./Nat. Fiber Optical Engineering Conf., San Diego, CA, USA, 2010, Paper OMI3.

[8] H. Xu, X. Li, X. Xiao, P. Zhou, Z. Li, J. Yu, and Y. Yu, “High-speed silicon modulator with band equalization,” *Opt. Lett.*, vol. 39, no. 16, pp. 4839–4842, 2014.

[9] M. R. Watts, W. A. Zortman, D. C. Trotter, R. W. Young, and A. L. Lentine, “Low-voltage, compact, depletion-mode, silicon Mach–Zehnder modulator,” *IEEE J. Sel. Topics Quantum Electron.*, vol. 16, no. 1, pp. 159–164, Jan./Feb. 2010.

[10] J. A. Dionne, K. Diest, L. A. Sweatlock, and H. A. Atwater, “PlasMOStor: A metal-oxide-Si field effect plasmonic modulator,” *Nano Lett.*, vol. 9, no. 2, pp. 897–902, 2009.

[11] A. Melikyan, N. Lindenmann, S. Walheim, P. M. Leufke, S. Ulrich, J. Ye, P. Vincze, H. Hahn, T. Schimmel, C. Koos, W. Freude, and J. Leuthold, “Surface plasmon polariton absorption modulator,” *Opt. Exp.*, vol. 19, no. 9, pp. 8855–8869, 2011.

[12] V. J. Sorger, N. D. Lanzillotti-Kimura, R.-M. Ma, and X. Zhang, “Ultra-compact silicon nanophotonic modulator with broadband response,” *Nanophoton.*, vol. 1, no. 1, pp. 17–22, 2012.

[13] E. Feigenbaum, K. Diest, and H. A. Atwater, “Unity-order index change in transparent conducting oxides at visible frequencies,” *Nano Lett.*, vol. 10, no. 6, pp. 2111–2116, 2010.

[14] J. Leuthold, C. Koos, W. Freude, L. Alloatti, R. Palmer, D. Korn, J. Pfeifle, M. Lauermann, R. Dinu, S. Wehrli, M. Jazbinsek, P. Gunter, M. Waldow, T. Wahlbrink, J. Bolten, H. Kurz, M. Fournier, J.-M. Fedeli, H. Yu, and W. Bogaerts, “Silicon-organic hybrid electro-optical devices,” *IEEE J. Sel. Topics Quantum Electron.*, vol. 19, no. 6, pp. 114–126, Nov./Dec. 2013.

[15] C. Koos, J. Leuthold, W. Freude, M. Kohl, L. Dalton, W. Bogaerts, A. L. Giesecke, M. Lauermann, A. Melikyan, S. Koeber, S. Wolf, C. Weimann, S. Muehlbrandt, K. Koehnle, J. Pfeifle, R. Palmer, L. Alloatti, D. Elder, T. Wahlbrink, and J. Bolten, “Silicon-organic hybrid (SOH) and plasmonic-organic hybrid (POH) integration,” presented at the Optical Fiber Communication Conf., Los Angeles, CA, USA, 2015, Paper Tu2A.1.

[16] C. Koos, J. Leuthold, W. Freude, L. Dalton, S. Koeber, R. Palmer, C. Weimann, D. Elder, W. Heni, D. Korn, J. Pfeifle, S. Wolf, D. Bekele, M. Woessner, L. Alloatti, P. Schindler, and S. Koenig, “Femtojoule modulation and frequency comb generation in silicon-organic hybrid (SOH) devices,” presented at the 16th Int. Conf. Trans. Optical Networks, Graz, Austria, 6–10, Jul. 2014, Paper We.C2.1.

[17] R. Palmer, L. Alloatti, D. Korn, P. C. Schindler, R. Schmogrow, W. Heni, S. Koenig, J. Bolten, T. Wahlbrink, M. Waldow, H. Yu, W. Bogaerts, P. Verheyen, G. Lepage, M. Pantouvaki, J. van Campenhout, P. Absil, R. Dinu, W. Freude, C. Koos, and J. Leuthold, “Silicon-organic hybrid MZI modulator generating OOK, BPSK and 8-ASK signals for up to 84 Gbit/s,” *IEEE Photon. J.*, vol. 5, no. 2, p. 6600907, Apr. 2013.

[18] C. Weimann, P. C. Schindler, R. Palmer, S. Wolf, D. Bekele, D. Korn, J. Pfeifle, S. Koeber, R. Schmogrow, L. Alloatti, D. Elder, H. Yu, W. Bogaerts, L. R. Dalton, W. Freude, J. Leuthold, and C. Koos, “Silicon-organic hybrid (SOH) frequency comb sources for terabit/s data transmission,” *Opt. Exp.*, vol. 22, no. 3, pp. 3629–3637, 2014.

[19] R. Palmer, S. Koeber, D. L. Elder, M. Woessner, W. Heni, D. Korn, M. Lauermann, W. Bogaerts, L. Dalton, W. Freude, J. Leuthold, and C. Koos, “High-speed, low drive-voltage silicon-organic hybrid modulator based on a binary-chromophore electro-optic material,” *J. Lightw. Technol.*, vol. 32, no. 16, pp. 2726–2734, Aug. 2014.

[20] S. Koeber, R. Palmer, M. Lauermann, W. Heni, D. L. Elder, D. Korn, M. Woessner, L. Alloatti, S. Koenig, P. C. Schindler, H. Yu, W. Bogaerts, L. R. Dalton, W. Freude, J. Leuthold, and C. Koos, “Femtojoule electro-optic modulation using a silicon–organic hybrid device,” *Light Sci. Appl.*, vol. 4, no. 2, p. e255, 2015.

[21] L. Alloatti, R. Palmer, S. Diebold, K. P. Pahl, B. Chen, R. Dinu, M. Fournier, J.-M. Fedeli, T. Zwick, W. Freude, C. Koos, and J. Leuthold, “100 GHz silicon-organic hybrid modulator,” *Light Sci. Appl.*, vol. 3, no. 5, p. e173, 2014.

[22] M. Lauermann, R. Palmer, S. Koeber, P. C. Schindler, D. Korn, T. Wahlbrink, J. Bolten, M. Waldow, D. L. Elder, L. R. Dalton, J. Leuthold, W. Freude, and C. Koos, “Low-power silicon-organic hybrid (SOH) modulators for advanced modulation formats,” *Opt. Exp.*, vol. 22, no. 24, pp. 29927–29936, 2014.

[23] M. Lauermann, S. Wolf, P. C. Schindler, R. Palmer, S. Koeber, D. Korn, L. Alloatti, T. Wahlbrink, J. Bolten, M. Waldow, M. Koenigsmann, M. Kohler, D. Malsam, D. L. Elder, P. V. Johnston, N. Phillips-Sylvain, P. A. Sullivan, L. R. Dalton, J. Leuthold, W. Freude, and C. Koos, “40 GBd 16QAM signaling at 160 Gb/s in a silicon-organic hybrid modulator,” *J. Lightw. Technol.*, vol. 33, no. 6, pp. 1210–1216, Mar. 2015.

[24] S. Wolf, M. Lauermann, P. Schindler, G. Ronniger, K. Geistert, R. Palmer, S. Köber, W. Bogaerts, J. Leuthold, W. Freude, and C. Koos, “DAC-less amplifier-less generation and transmission of QAM signals using sub-volt silicon-organic hybrid modulators,” *J. Lightw. Technol.*, vol. 33, no. 7, pp. 1425–1432, Apr. 2015.

[25] A. Melikyan, L. Alloatti, A. Muslija, D. Hillerkuss, P. C. Schindler, J. Li, R. Palmer, D. Korn, S. Muehlbrandt, D. van Thourhout, B. Chen, R. Dinu, M. Sommer, C. Koos, M. Kohl, W. Freude, and J. Leuthold, “High-speed plasmonic phase modulators,” *Nature Photon.*, vol. 8, no. 3, pp. 229–233, 2014.

[26] A. Melikyan, K. Koehnle, M. Lauermann, R. Palmer, S. Koeber, S. Muehlbrandt, P. C. Schindler, D. L. Elder, S. Wolf, W. Heni, C. Haffner, Y. Fedoryshyn, D. Hillerkuss, M. Sommer, L. R. Dalton, D. van Thourhout, W. Freude, M. Kohl, J. Leuthold, and C. Koos, “Plasmonic-organic hybrid (POH) modulators for OOK and BPSK signaling at 40 Gbit/s,” *Opt. Exp.*, vol. 23, no. 8, pp. 9938–9946, 2015.

[27] C. Haffner, W. Heni, Y. Fedoryshyn, J. Niegemann, A. Melikyan, D. L. Elder, B. Baeuerle, Y. Salamin, A. Josten, U. Koch, C. Hoessbacher, F. Ducry, L. Juchli, A. Emboras, D. Hillerkuss, M. Kohl, L. R. Dalton, C. Hafner, and J. Leuthold, “All-plasmonic Mach–Zehnder modulator enabling optical high-speed communication at the microscale,” *Nature Photon.*, vol. 9, pp. 525–528 2015.

[28] W. Heni, A. Melikyan, C. Haffner, Y. Fedoryshyn, B. Baeuerle, A. Josten, J. Niegemann, D. Hillerkuss, M. Kohl, D. Elder, L. Dalton, C. Hafner, and J. Leuthold, “Plasmonic Mach–Zehnder modulator with >70 GHz electrical bandwidth demonstrating 90 Gbit/s 4-ASK,” presented at the Optical Fiber Communication Conf., Los Angeles, CA, USA, 2015, Paper Tu2A.2.

[29] V. R. Almeida, Q. Xu, C. A. Barrios, and M. Lipson, “Guiding and confining light in void nanostructure,” *Opt. Lett.*, vol. 29, no. 11, pp. 1209–1211, 2004.

[30] R. Palmer, L. Alloatti, D. Korn, W. Heni, P. C. Schindler, J. Bolten, M. Karl, M. Waldow, T. Wahlbrink, W. Freude, C. Koos, and J. Leuthold, “Low-loss silicon strip-to-slot mode converters,” *IEEE Photon. J.*, vol. 5, no. 1, p. 2200409, Feb. 2013.

[31] L. Alloatti, M. Lauermann, C. Sürgers, C. Koos, W. Freude, and J. Leuthold, “Optical absorption in silicon layers in the presence of charge inversion/accumulation or ion implantation,” *Appl. Phys. Lett.*, vol. 103, no. 5, p. 051104, 2013.

[32] J. Pfeifle, L. Alloatti, W. Freude, J. Leuthold, and C. Koos, “Silicon-organic hybrid phase shifter based on a slot waveguide with a liquid-crystal cladding,” *Opt. Exp.*, vol. 20, no. 14, pp. 15359–15376, 2012.

[33] Y. Xing, T. Ako, J. George, D. Korn, H. Yu, P. Verheyen, M. Pantouvaki, G. Lepage, P. Absil, A. Ruocco, C. Koos, J. Leuthold, K. Neyts, J. Beeckman, W. Bogaerts, “Digitally controlled phase shifter using an SOI slot waveguide with liquid crystal infiltration,” *IEEE Photon. Technol. Lett.*, vol. 27, no. 12, pp. 1269–1272, Jun. 2015.

[34] D. Korn, M. Lauermann, P. Appel, L. Alloatti, R. Palmer, W. Freude, J. Leuthold, and C. Koos, “First silicon-organic hybrid laser at telecommunication wavelength,” presented at the Conf. Lasers Electro-Optics, San Jose, CA, USA, 2012, Paper CTu2I.1.

[35] D. A. B. Miller, “Energy consumption in optical modulators for interconnects,” *Opt. Exp.*, vol. 20, no. 102, pp. A293–A308, 2012.

[36] L. Alloatti, D. Korn, R. Palmer, D. Hillerkuss, J. Li, A. Barklund, R. Dinu, J. Wieland, M. Fournier, J. Fedeli, H. Yu, W. Bogaerts, P. Dumon, R. Baets, C. Koos, W. Freude, and J. Leuthold, “42.7 Gbit/s electro-optic modulator in silicon technology,” *Opt. Exp.*, vol. 19, no. 12, pp. 11841–11851, 2011.

[37] R. Ding, T. Baehr-Jones, Y. Liu, R. Bojko, J. Witzens, S. Huang, J. Luo, S. Benight, P. Sullivan, J.-M. Fedeli, M. Fournier, L. Dalton, A. Jen, and M. Hochberg, “Demonstration of a low V pi L modulator with GHz bandwidth based on electro-optic polymer-clad silicon slot waveguides,” *Opt. Exp.*, vol. 18, no. 15, pp. 15618–15623, 2010.

[38] D. L. Elder, S. J. Benight, J. Song, B. H. Robinson, and L. R. Dalton, “Matrix-assisted poling of monolithic bridge-disubstituted organic NLO chromophores,” *Chem. Mater.*, vol. 26, no. 2, pp. 872–874, 2014.

[39] Y. Jouane, Y-C. Chang, D. Zhang, J. Luo, A. K-Y. Jen, and Y. Enami, "Unprecedented highest electro-optic coefficient of 226 pm/V for electro-optic polymer/TiO2 multilayer slot waveguide modulators," *Opt. Exp.*, vol. 22, no. 22, pp. 27725–27732, 2014.

[40] J. Takayesu, M. Hochberg, T. Baehr-Jones, E. Chan, G. Wang, P. Sullivan, Y. Liao, J. Davies, L. Dalton, A. Scherer, and W. Krug, "A hybrid electrooptic microring resonator-based 1×4×1 ROADM for wafer scale optical interconnects," *J. Lightw. Technol.*, vol. 27, no. 4, pp. 440–448, Feb. 2009.

[41] P. A. Sullivan and L. R. Dalton, "Theory-inspired development of organic electro-optic materials," *Acc. Chem. Res.*, vol. 43, no. 1, pp. 10–18, 2010.

[42] L. R. Dalton, D. Lao, B. C. Olbricht, S. Benight, D. H. Bale, J. A. Davies, T. Ewy, S. R. Hammond, and P. A. Sullivan, "Theory-inspired development of new nonlinear optical materials and their integration into silicon photonic circuits and devices," *Opt. Mater.*, vol. 32, no. 6, pp. 658–668, 2010.

[43] L. R. Dalton, P. A. Sullivan, and D. H. Bale, "Electric field poled organic electro-optic materials: State of the art and future prospects," *Chem. Rev.*, vol. 110, no. 1, pp. 25–55, 2010.

[44] R. Palmer, L. Alloatti, D. Korn, P. C. Schindler, M. Baier, J. Bolten, T. Wahlbrink, M. Waldow, R. Dinu, W. Freude, C. Koos, and J. Leuthold, "Low power Mach–Zehnder modulator in silicon-organic hybrid technology," *IEEE Photon. Technol. Lett.*, vol. 25, no. 13, pp. 1226–1229, Jul. 2013.

[45] Y. V. Pereverzev, K. N. Gunnerson, O. V. Prezhdo, P. A. Sullivan, Y. Liao, B. C. Olbricht, A. J. P. Akelaitis, A. K.-Y. Jen, and L. R. Dalton, "Guest−host cooperativity in organic materials greatly enhances the nonlinear optical response," *J. Phys. Chem. C*, vol. 112, no. 11, pp. 4355–4363, 2008.

[46] Y. Enami, C. T. Derose, D. Mathine, C. Loychik, C. Greenlee, R. A. Norwood, T. D. Kim, J. Luo, Y. Tian, A. K.-Y. Jen, and N. Peyghambarian, "Hybrid polymer/sol–gel waveguide modulators with exceptionally large electro–optic coefficients," *Nature Photon.*, vol. 1, no. 3, pp. 180–185, 2007.

[47] F. Chang, K. Onohara, and T. Mizuochi, "Forward error correction for 100 G transport networks," *IEEE Commun. Mag.*, vol. 48, no. 3, pp. S48–S55, Mar. 2010.

[48] T. Baehr-Jones, R. Ding, Y. Liu, A. Ayazi, T. Pinguet, N. C. Harris, M. Streshinsky, P. Lee, Y. Zhang, A. E.-J. Lim, T.-Y. Liow, S. H.-G. Teo, G.-Q. Lo, and M. Hochberg, "Ultralow drive voltage silicon traveling-wave modulator," *Opt. Exp.*, vol. 20, no. 11, pp. 12014–12020, 2012.

[49] M. Lauermann, S. Wolf, R. Palmer, A. Bielik, L. Altenhain, J. Lutz, R. Schmid, T. Wahlbrink, J. Bolten, A. L. Giesecke, W. Freude, and C. Koos, "64 GBd operation of a silicon-organic hybrid modulator at elevated temperature," presented at the Optical Fiber Communication Conf., Los Angeles, CA, USA, 2015, Paper Tu2A.5.

[50] S. Wolf, P. C. Schindler, G. Ronniger, M. Lauermann, R. Palmer, S. Koeber, D. Korn, W. Bogaerts, J. Leuthold, W. Freude, and C. Koos, "10 GBd SOH modulator directly driven by an FPGA without electrical amplification," presented at the 40th European Conf. Optical Communication, Cannes, France, 2014, Paper Mo.4.5.4.

[51] R. Ding, T. Baehr-Jones, W.-J. Kim, B. Boyko, R. Bojko, A. Spott, A. Pomerene, C. Hill, W. Reinhardt, and M. Hochberg, "Low-loss asymmetric strip-loaded slot waveguides in silicon-on-insulator," *Appl. Phys. Lett.*, vol. 98, no. 23, p. 233303, 2011.

[52] W. Hartmann, M. Lauermann, S. Wolf, H. Zwickel, Y. Kutuvantavida, J. Luo, A. K.-Y. Jen, W. Freude, and C. Koos, "100 Gbit/s OOK using a silicon-organic hybrid (SOH) modulator," presented at the 41th European Conf. Optical Communication, Valencia, Spain, 2015, Paper PDP 1.4.

[53] J. P. Salvestrini, L. Guilbert, M. Fontana, M. Abarkanm, and S. Gille, "Analysis and control of the DC drift in $LiNbO_3$-based Mach–Zehnder modulators," *J. Lightw. Technol.*, vol. 29, no. 10, pp. 1522–1534, May 2011.

[54] W. Jin, P. V. Johnston, D. L. Elder, A. F. Tillack, B. C. Olbricht, J. Song, P. J. Reid, R. Xu, B. H. Robinson, and L. R. Dalton, "Benzocyclobutene barrier layer for suppressing conductance in nonlinear optical devices during electric-field poling," *Appl. Phys. Lett.*, vol. 104, pp. 243304–1–243304-3, 2014.

[55] L. R. Dalton, M. Jazbinsek, O. P. Kwon, P. Guenter, and P. A. Sullivan, in *Organic Electro-Optics and Photonics*. Cambridge, U.K.: Cambridge Univ. Press, 2015, pp. 1–293.

[56] A. F. Tillack, "Electro-optic material design criteria derived from condensed matter simulations using the level-of-detail coarse-graining approach," Ph.D. dissertation, Univ. Washington, Seattle,WA, USA, 2015.

[57] L. E. Johnson, L. R. Dalton, and B. H. Robinson, "Optimizing calculations of electronic excitations and relative hyperpolarizabilities of electrooptic chromophores," *Acc. Chem. Res.*, vol. 47, no. 11, pp. 3258–3265, 2014.

[58] P. A. Sullivan and L. R. Dalton, "The materials genome for organic electro-optics and silicon/plasmonic—organic hybrid technology," in *New Horizons in Nanoscience and Engineering*, D. L. Andrews and J. G. Grote, Eds. Bellingham, WA, USA: SPIE Press, pp. 233–284, 2015.

[59] L. R. Dalton, M. Lauermann, and C. Koos, "Nonlinear optics: Electro-optic applications," in *The WSPC Reference on Organic Electronics: Organic Semiconductors*, vol. 7, J.-L. Bredas and S. R. Marder, Eds. Singapore and London: World Scientific and Imperial College Press, 2015, ch. 13.

[60] R. Soref and B. Bennett, "Electrooptical effects in silicon," *IEEE J. Quantum Electron.*, vol. 23, no. 1, pp. 123–129, Jan. 1987.

[61] C. Koos, *Nanophotonic Devices Linear Nonlinear Optical Signal Processing*,. Karlsruhe, Germany: Univ.-Verl. Karlsruhe, 2007.

Authors' biographies are not available at the time of publication.

QUERIES

Q1. Author: Please check the name of all authors for correctness.